

Broadband ferromagnetic resonance measurements on thin cobalt films at low temperatures

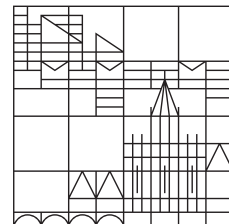
Master's Thesis

by

Oliver Irtenkauf

at the

Universität
Konstanz



Faculty of Science
Department of Physics

1. Reviewer: Prof. Dr. Elke Scheer
2. Reviewer: Prof. Dr Angelo Di Bernardo

Konstanz, 2021

Zusammenfassung

Es ist bekannt, dass durch ferromagnetische Resonanz (FMR) Anregungen ein reiner Spinstrom aus einem präzidierenden Ferromagneten (F) in ein normales Metall (N) eingekoppelt werden kann. Dieser Spinstrom kann in spintronischen Bauelementen zur Kodierung und Verarbeitung digitaler Informationen genutzt werden.

Ähnlich wie im Fall von F/N-Systemen wurde kürzlich vorgeschlagen, dass ein vollständig spinpolarisierter (Spin-Triplett) supraleitenden Strom (Suprastrom) auch in Supraleiter/Ferromagneten (S/F) Systemen erzeugt werden kann und somit zur Nutzung von Spintronik-Operationen mit geringen Energieverlusten im supraleitenden Regime eingesetzt werden kann. Im Gegensatz zu konventionellen Supraströmen, die aus antiparallel ausgerichteten (Spin-Singulett) Cooper-Paaren von Elektronen bestehen, sind Spin-Triplett Supraströme nicht nur spinpolarisiert, sondern auch langreichweitig innerhalb eines F. Folglich könnte man durch Realisierung eines S/F/S-Josephson-Bauelements und Anregung einer FMR der F-Schicht von einem Zustand, in dem kein Transport zwischen den beiden S-Schichten stattfindet (aufgrund des schnellen Abklingens des Spin-Singlet Suprastroms in F), zu einem Zustand wechseln, in dem die beiden S-Schichten stattdessen über einen Spin-Triplett Suprastrom gekoppelt sind, der durch die FMR-Anregung von F ausgelöst wird. Um solche supraleitenden Bauelemente zu realisieren, die über FMR-Anregung geschaltet werden können, scheint es entscheidend zu sein, das FMR-Signal von ultradünnen F-Schichten auslösen und detektieren zu können.

Basierend auf diesen Beweggründen wird in dieser Arbeit ein Aufbau zur hochempfindlichen Messung des FMR-Signals von ultradünnen Co (F)-Schichten (bis zu $\approx 3 \text{ nm}$ Dicke) diskutiert. Die ultradünnen Co-Schichten werden durch Elektronenstrahlverdampfung erzeugt, gefolgt von der Herstellung eines koplanaren Wellenleiters darauf. Mikrowellentransmissionsmessungen werden bei niedrigen Temperaturen unter Verwendung eines in der Ebene liegenden Magnetfeldes und eines breitbandigen Vektornetzwerkanalysators durchgeführt. Eine quantitative Beziehung zwischen der FMR Frequenz und dem angelegten Magnetfeld wird hergestellt. Die Funktionsweise des Aufbaus einschließlich seiner Optimierung in Bezug auf die Rauschunterdrückung des FMR-Signals wird diskutiert. Die erzielten Ergebnisse zeigen die Eignung des Aufbaus für die Charakterisierung der Transporteigenschaften von S/F/S-Bauteilen unter FMR-Anregung.

Abstract

It is well-established, that through ferromagnetic resonance (FMR) excitation a pure spin current can be injected from a precessing ferromagnet (F) into a normal metal (N) material. This spin current can be used in spintronic devices for the encoding and processing of digital information.

Similar to the case of F/N systems, very recently it has been suggested that a fully spin-polarized (spin-triplet) superconducting current (supercurrent) can be generated also in superconductor/ferromagnet (S/F) systems, and therefore applied to perform spintronics operations with low energy dissipation in the superconducting regime. Unlike conventional supercurrents that consist of antiparallel-aligned (spin-singlet) Cooper pairs of electrons, spin-triplet supercurrents are not only spin-polarized but also long-ranged inside a F. As a result, by realizing a S/F/S Josephson device and exciting a FMR of the F layer, one could switch from a state where no transport occurs between the two S layers (due to the quick decay of the spin-singlet supercurrent in F) to a state where the two S layers are instead coupled via a spin-triplet supercurrent triggered via the FMR excitation of F. To realize such superconducting devices, which can be switched via FMR excitation, it appears crucial to be able to trigger and detect the FMR signal from ultrathin F layers.

Based on these motivations, in this thesis a setup for high-sensitivity measurement of the FMR signal from ultrathin Co (F) thin films (down to $\approx 3\text{ nm}$ in thickness) is discussed. The ultrathin Co thin films are grown by electron beam evaporation followed by the fabrication of a co-planar waveguide on top of them. Microwave transmission measurements are performed at low temperatures, using an in-plane magnetic field and a broadband vector network analyzer. A quantitative relation between FMR frequency and applied magnetic field is derived. The performance of the setup including its optimization in terms of noise reduction of the FMR signal is discussed. The results obtained demonstrate the suitability of the setup for the characterization of the transport properties of S/F/S devices under FMR excitation.

Kleines Statement ¹

Hineinfließen
in die Formen,
die sich stellen.
Sich aber nicht
formen lassen
und auf keinen Fall
erhärten.

Das wäre
Leben
für mich.

¹Kristiane Allert-Wybranietz (*1955)

Contents

1	Introduction	1
2	Theory	2
2.1	Landau-Lifshitz-Gilbert Model	2
2.2	Kittel Formula	4
2.3	Co-planar Waveguide	5
2.4	Coherence Lengths	5
2.5	State of the Art of Research	7
3	Setup and Samples	8
3.1	Sample Design and Preparation	8
3.2	Setup	9
4	Technical Findings	12
4.1	Data Processing	13
4.2	Modeling	16
4.3	Signal Optimization	18
4.3.1	HelioxVL Setup Magnetization	18
4.3.2	Comparison of the Setups Used	19
4.3.3	Magnetic Field and Frequency Sweep method	19
4.3.4	Noise Induced by the Laboratory Temperature	21
4.3.5	Parameter Study	23
4.4	Frequency Domain Reflectometry	23
4.5	Transmission Dependency on Sample Temperature	25
5	Results and Diskussion	27
6	Conclusion	30
Appendix		i
List of Figures		x
References		xi

1 Introduction

The field of spintronics utilizes the targeted manipulation of spin currents. The goal is to build devices with high energy efficiency either for large computer clusters or for quantum mechanical applications. The physical concept of superconductivity comes in handy at this point, but raises the question of how to specifically manipulate the spin of the superconducting current (supercurrent). As a consequence, the interface between superconductor (S) and ferromagnet (F) is of great interest.

When considering conventional superconductivity, according to Bardeen, Cooper & Schrieffer [1], Cooper pairs consist of two electrons with opposite momentum and spin. Due to the total spin $S = 0$ rapid dephasing of the Cooper pair occurs in ferromagnets within only a few nanometers and therefore long-range supercurrents are forbidden within them.

However, according to Fulde, Ferrel, Larkin & Ovchinnikov [2, 3] Cooper pairs can come in triplet states with total spin $S = 1$. Antiparallel spin pairs ($S_z = 0$) oscillate in the external magnetic field between antiparallel singlet and triplet states during their rapid dephasing. An external magnetic field has no pair-breaking effect on parallel triplet pairs ($S_z = \pm 1$), resulting in much slower dephasing, which is why they are also called long-range spin triplets. A schematic of the different Cooper pairs is shown in Figure 1. As a consequence, a ferromagnet of sufficient size can be used as a spin polarizer for supercurrents if long-range spin triplets are present.

Besides the static excitation of spin-triplet pairs by complex interlayers [4, 5, 6, 7], this should also be possible in a dynamical system by magnon absorption. This was predicted by Hikino et al. [8, 9] and provided with evidence by Jeon et al. [10]. Subsequently, this means that a long-range spin current can be induced through a S/F/S Josephson contact by microwave irradiation at the frequency of ferromagnetic resonance (FMR) without the need for special interface preparation.

In summary, I am interested in the ferromagnetic properties of such an S/F/S contact. In this thesis I share with you my results on resolving the FMR of thin Co films with broadband measurements at different in-plane magnetic fields and cryogenic temperatures.

First, I will recall magnetization dynamics theory that leads to the description of FMR. Then, I will present the samples and the setups used in my experiments. Next, I will present my more technical findings related to encountered technical problems during my measurements. Finally, I will also discuss the magnetization properties obtained by FMR measurements.

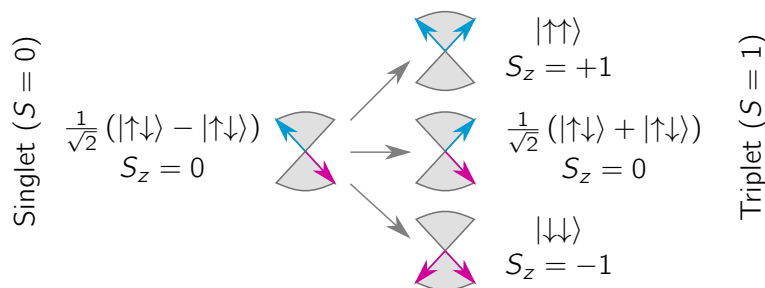


Figure 1 Schematic of the singlet ($S = 0$) and triplet ($S = 1$) Cooper pair states. The precession cones of the spins in the externally applied magnetic field along z are shown in grey and the two single spins in magenta and blue. Depending on their orientation, the total spin of a Cooper pair can have a finite $S_z = \pm 1$ or vanishing z -component $S_z = 0$. [7]

2 Theory

In this Chapter in order to understand the ferromagnetic resonance (FMR) technique I want to recall some basic concepts of magneto dynamics. Furthermore, I also want to give a short excursion into the coherence lengths of singlet and triplet Cooper pairs, since they are needed to define my samples dimensions reasonably. Finally, I want to present you the current state of the art, in the field of FMR measurements on thin ferromagnetic films.

2.1 Landau-Lifshitz-Gilbert Model

The dynamic magnetic properties of a ferromagnet can be described by damped precessional motion of the exchange-coupled magnetic moments. If the externally applied magnetic fields and excitation energies are significantly smaller than the exchange coupling energy, we can describe the whole ferromagnet as a macroscopic magnetic spin by the Landau-Lifshitz-Gilbert (LLG) model. [11, 12]

The LLG differential equation for the magnetization \mathbf{M} is given by

$$\frac{d\mathbf{M}}{dt} = \underbrace{-|\gamma|(\mathbf{M} \times \mu_0 \mathbf{H}_{\text{eff}})}_{(1)} + \underbrace{\frac{\alpha}{|\mathbf{M}|} \left(\mathbf{M} \times \frac{d\mathbf{M}}{dt} \right)}_{(2)}, \quad (2.1)$$

where γ is the gyro-magnetic ratio, α is the Gilbert damping parameter and μ_0 is the vacuum permeability. The effective magnetic field is given by $\mathbf{H}_{\text{eff}} = \mathbf{H} + \mathbf{H}_{\text{ani}}$, with \mathbf{H} being the externally applied magnetic field and \mathbf{H}_{ani} the anisotropy field.

For better understanding of the LLG model, we first neglect the Gilbert damping term (2) in equation 2.1. With this neglection the LLG equation simply describes the precession of the magnetization \mathbf{M} around the effective field \mathbf{H}_{eff} . Here the gyro-magnetic ratio is given by $\gamma_e = \frac{g_e \mu_B}{\hbar} = \frac{g_e q_e}{2m_e}$, where \hbar is the reduced Planck constant, μ_B the Bohr magneton, g_e , q_e and m_e describe the g -factor, charge and mass of the free electron respectively. Since the magnetism in ferromagnets, especially in Co, is caused by the electron spins, we can assume a g -factor $g \approx 2$ and thus a gyromagnetic ratio of $\frac{\gamma}{2\pi} = 28.025 \text{ GHz T}^{-1}$. The precession frequency ω_{res} is given by

$$\omega_{\text{res}} = \gamma \mu_0 |\mathbf{H}_{\text{eff}}|, \quad (2.2)$$

resulting in typical resonance frequencies $\omega_{\text{res}}/2\pi$ in the GHz range, for a few Tesla of applied external magnetic field.

Now we consider the phenomenological Gilbert term (2) from equation 2.1. After the displacement of \mathbf{M} , it precesses in a spiral trajectory back to its equilibrium position. This relaxation is due to the scattering of phonons and magnons and can be characterised by the relaxation rate κ . This rate is related to the frequency linewidth by $\Delta\omega = \frac{1}{2\kappa}$, where the linewidth $\Delta\omega$ is usually defined as full width at half maximum (FWHM) and κ as the inverse of the half width at half maximum (HWHM). Now the linewidth $\Delta\omega$ is connected to the Gilbert parameter α by

$$\Delta\omega = 2\alpha\omega_{\text{res}} + \Delta\omega_0. \quad (2.3)$$

The inhomogeneous broadening $\Delta\omega_0$ is caused by magnetic inhomogeneities or surface effects. [13]

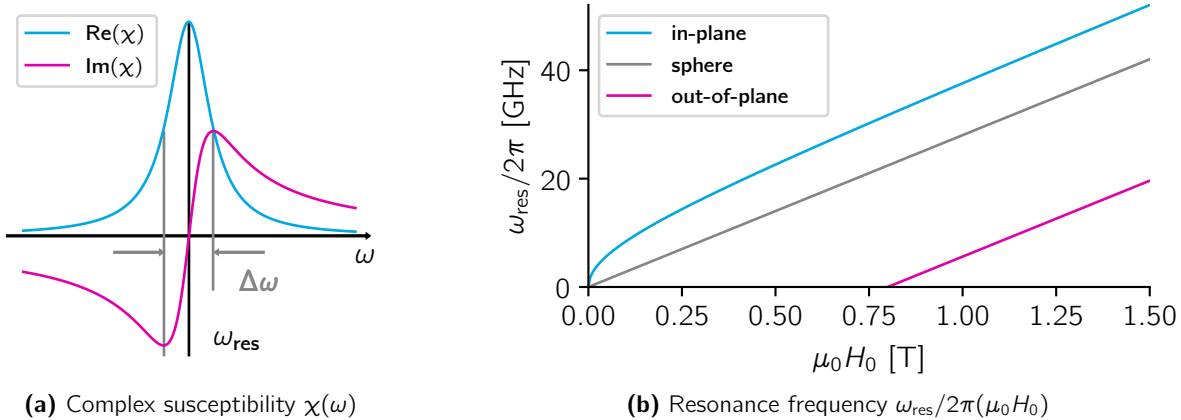


Figure 2 (a) Schematic of the complex Polder susceptibility $\chi(\omega)$ in arbitrary units, according to equation 2.7. The maximum of the real part (blue) and the zero crossing of the imaginary part (magenta) are marking the resonance frequency ω_{res} . The FWHM of the real part and the distance between the minimum and maximum of the imaginary part is marking the line width $\Delta\omega$.

(b) Simulation of the ferromagnetic resonance frequency $\omega_{\text{res}}/2\pi(\mu_0 H_0)$, according to equation 2.10-2.12. Shown are the curves for the three most common shape anisotropies, that of a sphere (grey), an in-plane (blue) or an out-of-plane (magenta) magnetized thin film. Parameters: $M_0 = 8 \text{ kOe}$ & $\gamma = 28.025 \text{ GHz T}^{-1}$

In order to solve the LLG differential equation 2.1 we will neglect for now the field anisotropy $\mathbf{H}_{\text{ani}} = 0$. To this end we split the applied magnetic field \mathbf{H} and magnetization \mathbf{M} into static ($\mathbf{H}_0, \mathbf{M}_0$) and dynamic (\mathbf{h}, \mathbf{m}) components.

$$\mathbf{H} = \mathbf{H}_0 + \mathbf{h}(t) \quad (2.4)$$

$$\mathbf{M} = \mathbf{M}_0 + \mathbf{m}(t) \quad (2.5)$$

Next we assume a static magnetic field in z -direction and a dynamic field in x - and y -direction $\mathbf{H} = (h_x(t), h_y(t), H_0)$. If the dynamic magnetic field is much smaller than the static magnetic field, we can also write for the magnetization $\mathbf{M} = (m_x(t), m_y(t), M_0)$. Here is M_0 the absolute static magnetization. The solution is given by $\mathbf{m} = \boldsymbol{\chi}\mathbf{h}$. The two-dimensional Polder tensor $\boldsymbol{\chi}$ is given by

$$\boldsymbol{\chi} = \begin{pmatrix} \chi_{11} & i\chi_{12} \\ -i\chi_{12} & \chi_{22} \end{pmatrix}. \quad (2.6)$$

[14]

Since we neglect magnetic field anisotropy, the diagonal elements are the same $\chi = \chi_{11} = \chi_{22}$. Further, we neglect every higher damping term $\mathcal{O}(\alpha^2)$, in order to get the linear response of a ferromagnet in an external field. Finally, the Polder susceptibility is then given by

$$\chi(\omega, H_0) = \frac{\omega_M (\gamma\mu_0 H_0 - i\Delta\omega)}{(\omega_{\text{res}}(H_0))^2 - \omega^2 - i\omega\Delta\omega}. \quad (2.7)$$

Here is the magnetization frequency $\omega_M = \gamma\mu_0 M_0$ and the resonance frequency ω_{res} . In Figure 2a, you can see the qualitative behaviour of the Polder susceptibility $\chi(\omega)$ around the resonance frequency ω_{res} . [15, 16]

2.2 Kittel Formula

Most macroscopic ferromagnets have two opposite favorable directions in which they are most easily magnetized. The so-called easy-axis, which is parallel to the two directions, can be of different origin. In the following simplest case the sample shape anisotropy is treated. Here the magnetic field \mathbf{H} can be written as follows:

$$\mathbf{H} = \mathbf{H}_0 + \mathbf{H}_{\text{demag}} + \mathbf{h}(t). \quad (2.8)$$

The demagnetization field is given by $\mathbf{H}_{\text{demag}} = \mathbf{N} \cdot \mathbf{M}$, where the spatially independent demagnetization tensor \mathbf{N} is in diagonal form, with elements $N_{x,y,z}$. The resonance frequency can be written as

$$\omega_{\text{res}} = \gamma\mu_0\sqrt{(H_0 + (N_y - N_z)M_0)(H_0 + (N_x - N_z)M_0)}, \quad (2.9)$$

if the applied magnetic field is in the direction of the z -axis.

These demagnetisation factors $N_{x,y,z}$ are strongly dependent on the sample geometry. The three most common geometries are discussed below.

1. spherical geometry ($N_{x,y,z} = 1/3$).

$$\omega_{\text{res}}^{\circ} = \gamma\mu_0 H_0 \quad (2.10)$$

2. thin out-of-plane magnetized film ($N_{x,y} = 0, N_z = 1$).

$$\omega_{\text{res}}^{\perp} = \gamma\mu_0(H_0 - M_0) \quad (2.11)$$

3. thin in-plane magnetized film ($N_{x,z} = 0, N_y = 1$).

$$\omega_{\text{res}}^{\parallel} = \gamma\mu_0\sqrt{H_0(H_0 + M_0)} \quad (2.12)$$

The ferromagnetic resonance frequencies are simulated in Figure 2b.

If there are no other anisotropies than shape anisotropy, M_0 is replaced by the saturation magnetization M_s . [17]

If uniaxial field anisotropy is present, H_0 is replaced by $H_{\text{eff}} = H_0 + H_{\text{ani}}$. For thin in-plane magnetized films, the uniaxial field anisotropy is typically on the order of a few mT. [16]

At this point, it should be noted that we do not know with certainty whether the easy-axis in thin Co films is in-plane, because out-of-plane easy-axis is also possible. With a suitable substrate, such as Au or Pt, single-digit monolayers of Co, and a suitable cap, such as Au or Ag, out-of-plane magnetization of Co may be present. In addition, there are studies of Co films as thin as 40 nm that both at normal and oblique incidence of atomic current during electron beam evaporation Co always exhibit in-plane easy-axis. At this point, I suspect that Co exhibits robust in-plane magnetization and only shows out-of-plane magnetization under very special conditions. [18, 19, 20, 21]

Furthermore, it should be considered that superconductors, such as aluminum, have a critical magnetic field of only a few mT. Only for very thin films, in the single-digit nanometer range, aluminum can achieve an in-plane critical field in the Tesla range. To use a finite ferromagnetic resonant frequency, within the critical magnetic field, an in-plane geometry must be used. [22, 23]

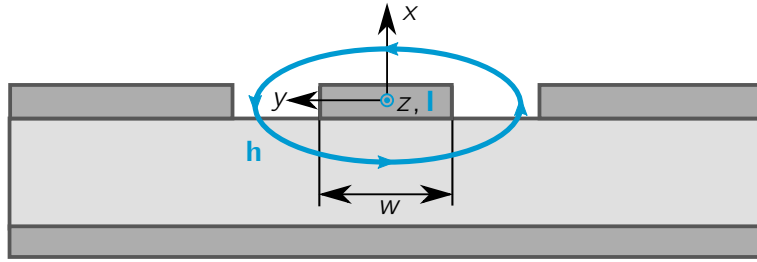


Figure 3 Cross-section schematic of a co-planar wave guide. The laboratory reference frame is centered on the inner conductor with width w and infinitesimal height. The magnetic field \mathbf{h} curves around the current I right-handed wise. Whereas the dark grey areas are conducting, the light grey area is insulating. The conducting area beside and below the inner conductor are separated by an insulating layer and connected to ground.

2.3 Co-planar Waveguide

In order to generate an alternating magnetic field distribution \mathbf{h} I use a co-planar wave guide (CPW). The CPW consists of an inner conductor, with width w , an infinitesimal height and two neighboring ground pads. For further descriptions I use the laboratory reference frame, shown in Figure 3, with x perpendicular to the CPW plane, z in direction of the inner conductor and y being perpendicular to x and z .

For an infinitely thin sheet the field distribution h_0 at the position $(x, y) = (0, 0)$, the middle of the inner conductor, can be related to the current density j or the current I , by

$$h_0 = \frac{j}{2} = \frac{I}{2w}. \quad (2.13)$$

We also assume that the ground pads are infinitely large and so the current density through them is converging to zero.

Furthermore, we are interested in the field distribution $\mathbf{h}(x, y)$ in the x - y -plane. In vacuum, meaning with relative magnetic permittivity $\mu = 1$, we can approximate this situation with the Karlqvist equations [24], given by

$$h_y(x, y) = \frac{h_0}{\pi} \left[\text{atan} \left(\frac{y + w/2}{x} \right) - \text{atan} \left(\frac{y - w/2}{x} \right) \right] \quad (2.14)$$

$$h_x(x, y) = \frac{h_0}{2\pi} \ln \left[\frac{(y + w/2)^2 + x^2}{(y - w/2)^2 + x^2} \right]. \quad (2.15)$$

These equations neglect the presence of the ground pads and a solution is visualized in Figure 4.

For good electrical transmission through the CPW, its impedance must match to the impedance of the cabling. The impedance of the CPW can be adjusted by the width of the CPW's inner conductor and its distance to the ground pad. For more information see textbooks on high frequency technology. [25, 26]

2.4 Coherence Lengths

The supercurrent through a superconductor/ferromagnet/superconductor (S/F/S) contact depends essentially on the thickness of the ferromagnet. However, this thickness affects the magnetic properties, which in turn determine the FMR. In general, we want to design an S/F/S contact, so we can measure a difference in electronic transport for short-range singlet and long-range triplet superconductivity. To this end, we consider the corresponding decay lengths in the ferromagnet.

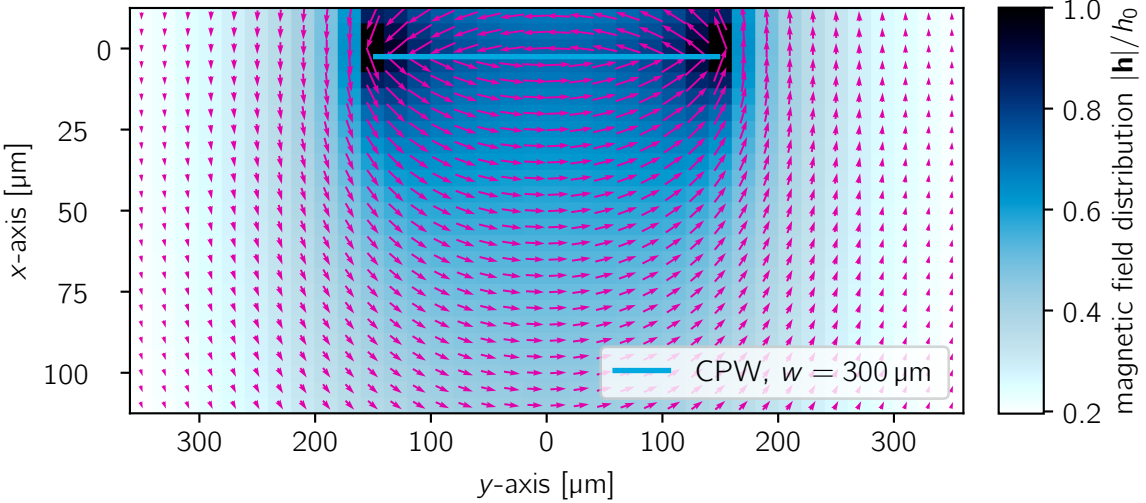


Figure 4 Magnetic field distribution $\mathbf{h}(x, y)$ of a CPW according to Karlqvist equations 2.14 & 2.15. In blue you can see the infinitely thin inner conductor of a CPW, with width $w = 300 \mu\text{m}$. However, the ground pads are neglected. The magenta arrows are indicating the direction, whereas their length and the color scale are indicating the absolute magnetic field $|\mathbf{h}(x, y)|/h_0$.

For singlet superconductivity we are interested in the superconducting correlation decay length in a ferromagnet ξ_f . For this purpose, we assume diffusive transport, i.e., the mean free path ℓ of the electron scattering is small compared to the coherence length. This is the case if there are many defects in the lattice, also called the dirty limit. The diffusion constant is given by $D_f = \frac{1}{3}v_F\ell$, where v_F is the Fermi velocity. Considering the exchange field h_{ex} , we can write

$$\xi_f = \sqrt{\frac{D_f}{h_{\text{ex}}}} = \sqrt{\frac{\hbar v_F \ell}{3h_{\text{ex}}}}. \quad (2.16)$$

For Co the electron-scattering mean free path is given by $\ell_{\text{Co}} = 7.8 \text{ nm}$, whereas the exchange field is given by $h_{\text{ex, Co}} = 5.15 \cdot 10^{-21} \text{ J}$. This results in a decay length of $\xi_{f, \text{Co}} = 3.7 \text{ nm}$. [27, 28, 29]

The penetration depth of long-range triplet pairs $\xi_\epsilon = \sqrt{\frac{D_f}{\epsilon}}$ into the ferromagnet, is of the same order as the penetration depth of singlet pairs into a normal conductor $\xi_\epsilon \approx \xi_n$. In practice, we replace the energy term ϵ by the thermal energy $k_B T$ and multiply a factor of 2π . This leads to the approximation

$$\xi_n = \sqrt{\frac{\hbar v_F \ell}{6\pi k_B T}}. \quad (2.17)$$

Again, the mean free path of electron scattering for Co is $\ell_{\text{Co}} = 7.8 \text{ nm}$ and we assume a temperature of $T = 300 \text{ mK}$. This temperature only has to be smaller than the critical temperature of the superconductor used, aluminum $T_c, \text{Al} = 1, 2 \text{ K}$ and is reasonably achievable with the used setup. Taking this into account, the decay length for long-range triplet pairs is $\xi_{n, \text{Co}}(T = 300 \text{ mK}) = 52 \text{ nm}$. [20, 28, 30, 31]

In summary, the thickness of the Co should now be somewhere between 3.7 and 52 nm to measure a significant difference in electronic transport between singlet and triplet superconductivity. However, a lower Co thickness of, say, 3 nm, can also be advantageous. On the one hand, singlet superconductivity can be studied very well, on the other hand, the effect of triplet superconductivity will still be easy to observe.

2.5 State of the Art of Research

In this Section I will focus on the presentation of publications related to broadband (bb) ferromagnetic resonance (FMR) measurements on thin magnetic films. As a quick reminder I use a 2-port vector network analyzer (VNA) and couple my thin Co films with a co-planar waveguide (CPW) at cryogenic temperatures (0.1 to 4 K) and in-plane magnetic fields.

Kalarickal et al. present various relative broadband FMR methods and the resulting determination of the Gilbert damping with it of thin (50 to 100 nm) in-plane permalloy layers. It is found that the methods strip-line FMR, VNA FMR and pulsed inductive microwave magnetometer give comparable results. [16]

Maier-Flaig et al. also deal with the characterization of thin permalloy films. The CPW VNA technique is also used, but the magnetic field is applied out-of-plane. This allows the clever application of numerical methods for background treatment. Thus, uncalibrated measurements can be made and noise can be removed afterwards. [32, 33]

Tamaru et al. deal with the signal enhancement of VNA FMR by additionally modulating the in-plane applied magnetic field in the Hertz frequency range. A CPW and a stack of FeB(1.6 nm)/W(0.1 nm)/FeB(1.1 nm) were used for this purpose. [34]

Harward et al. have developed a bbFMR system with impressive 10 MHz to 70 GHz frequency bandwidth. Furthermore, they can vary the sample temperature from 27 to 350 K. They claim to achieve a sensitivity of less than one monolayer of crystalline iron. For their measurement they use a CPW and can apply the magnetic field simultaneously in- and out-of-plane. [35]

Denysenkov and Grishin report a strip-line bbFMR setup in a cryostat (4 to 420 K). This allowed them to resolve the signal of YIG films with 1 μm thickness. The magnetic field can be applied in-plane or out-of-plane through a rotatable sample holder. [36]

Bilzer et al have studied the use of all four possible scattering parameters of a 2-port VNA. They were able to determine the resonance frequency with only the forward transmission scattering parameter with less than one percent deviation compared to all four scattering parameters used. A CPW and a 40 nm thick in-plane permalloy film were used. [37]

In summary, permalloy was mostly used for good signal-to-noise ratio. It was found that the CPW VNA bbFMR method gives equivalent results to other bbFMR methods. The number of scattering parameters used is not important. It is possible to implement these methods for in- or out-of-plane magnetic fields and at cryogenic temperatures.

3 Setup and Samples

In this Chapter I will introduce the design and preparation of my samples. Then I will introduce the cryostats and magnets, the vector network analyzer including signal pre-amplifier, and finally discuss the sample holder and cabling used in my experiments.

3.1 Sample Design and Preparation

First, as already shown in Chapter 2.4, the thickness of the Co should be somewhere between 3.7 to 52 nm to be able to measure a significant difference in electronic transport between singlet and triplet superconductivity. At the same time I prefer a sample volume as large as possible, since a large volume also means a considerable absorption and thus a ferromagnetic resonance (FMR) signal. Therefore, it seemed advisable to start with a Co layer of 30 nm.

To complete the superconductor/ferromagnet/superconductor (S/F/S) contact, I use 100 nm Al each to sandwich the Co. Here I study the thicknesses already used by Andreas Bloch for the electronic transport measurement optimized samples.

Since we are also interested in transport measurements through the S/F/S contact, we had to prevent it from being short-circuited. Therefore, the S/F/S contact must be electrically isolated from the co-planar wave guide (CPW) on top. This was achieved by an intermediate polyimide (PI) layer.

The CPW on the top of the samples consists of an inner conductor and ground pads. It is composed of a thin layer of Ti for good adhesion with a thick layer of Au for high conductivity on top. Figure 5d shows a schematic diagram of the top view and the dimensions used.

The samples CPW1 (Figure 5a) and CPW2 (Figure 5b) consist of a S/F/S sandwich structure of Al/Co/Al, a PI layer and a Ti/Au CPW on top. They differ slightly in the Co thickness and in the lateral extent of the Al/Co/Al sandwich. While the sandwich on the CPW1 sample is extended over the whole chip, the sandwich on the CPW2 sample is structured in the shape of the CPW.

It has turned out that smaller layers of Co, such as 3 nm, are also very interesting. Here singlet superconductivity can be studied easily, but also the effect of triplet superconductivity will be investigable. The sample CPW3 (Figure 5c) consists of a single sandwich in the shape of the CPW. At the very bottom is a 3nm Co layer directly on the wafer to get the Co layer as continuous as possible. On top of that is a Cu¹ layer and a Ti/Au CPW.

Now I would like to go through the preparation steps using sample CPW2. Used parameters can be found in Table 2, in the Appendix. For photo-lithography a layer of photoresist is deposited on a Si wafer. The resist is exposed to UV light in the form of the CPW by the mask-less photo-lithography tool. The resist is then developed and the sample is covered with the Al/Co/Al sandwich either by thermal or electron-beam evaporation. During lift-off, the remaining resist layer with the Al/Co/Al sandwich on top comes off. Now an Al/Co/Al sandwich structure in the form of a CPW remains. After applying a PI layer, the lithography process just described is repeated for a Ti/Au layer instead of Al/Co/Al.

¹Cu was used to rule out Zeeman splitting in aluminum, as a cause of parts of the signal. However, hypothesis of Zeeman splitting was proven to be wrong.

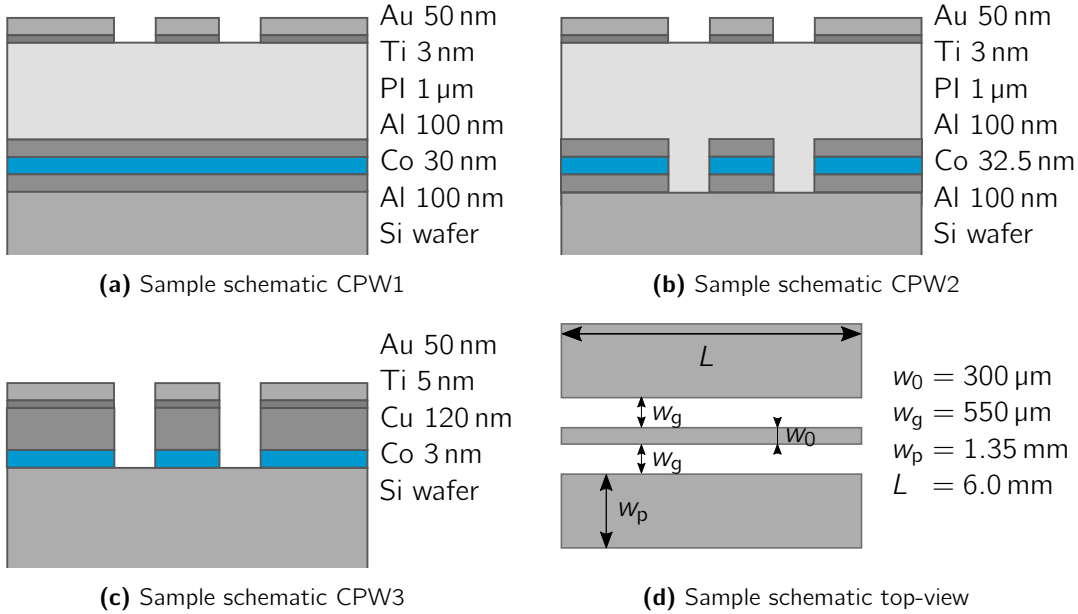


Figure 5 Schematics of the different sample designs. **(a)**, **(b)** & **(c)** are showing the cross-sections of the samples CPW1, CPW2 & CPW3. On each right side, the different materials and thicknesses are written. In **(d)** you can see a top-view of the used wave guide mask and its dimensions. These dimensions are used for all my samples.

3.2 Setup

In this Section I want to describe the two setups 'BlueFors' and 'HelioxVL', I used. A schematic for each setup can be found in Figure 6. A list of the used devices, can be found in Table 1.

The BlueFors setup consists of a cryogen-free dilution refrigerator system with and a superconducting magnet. A large number of thermometers are also installed, although only two of them are used for measurements. One thermometer is installed in the magnet (T_{magnet}), the other one is mounted close to the sample holder (T_{FMR}), see Figure 7a and has already been calibrated by Martin Prestel.

The cabling from the mixing chamber (MXC) to the sample holder was done previously by Sergej Andreev. At the 50 K stage, a damper for each measurement line with -10 dB is mounted. Between the 4 K stage and the MXC, high-temperature superconducting cables are used. This choice ensures good electrical contact and reduces thermal contact between the stages. Additionally, connectors are screwed into each stage to ensure thermalization of the cables. Between mixing chamber and sample holder copper coaxial cables are used to ensure good thermal flow towards the sample. The sample holder is designed in such a way, that the inner conductor is simply pressed onto a PCB board. This procedure avoids ferromagnetic contamination by the typically used connectors. The PCB board clamps the sample down and connects the CPW to the high-frequency cables by CuBe alloy clamps. You can see a picture of the sample holder in Figure 7a.

The HelioxVL setup in a wet cryostats, consisting of a ^3He sample-in-vacuum dipstick and a dewar with built-in superconducting magnet. A thermometer is attached to the sample holder. The high-frequency cabling and the sample holder shown in Figure 7b were realized in advance by Andreas Bloch and Lukas Kammermeier. The high-frequency cabling consist of copper cables for all setup parts with operating temperatures down to 4 K. For all parts with lower operating temperatures superconducting high frequency cables consisting of Nb/Ti are used.

The vector network analyzer (VNA) and pre-amplifier are mounted on a mobile rack for easy switching between setups. In addition, the room temperature thermometer and a measurement PC are mounted.

The VNA, both magnets, the room temperature thermometer and the thermometer of the

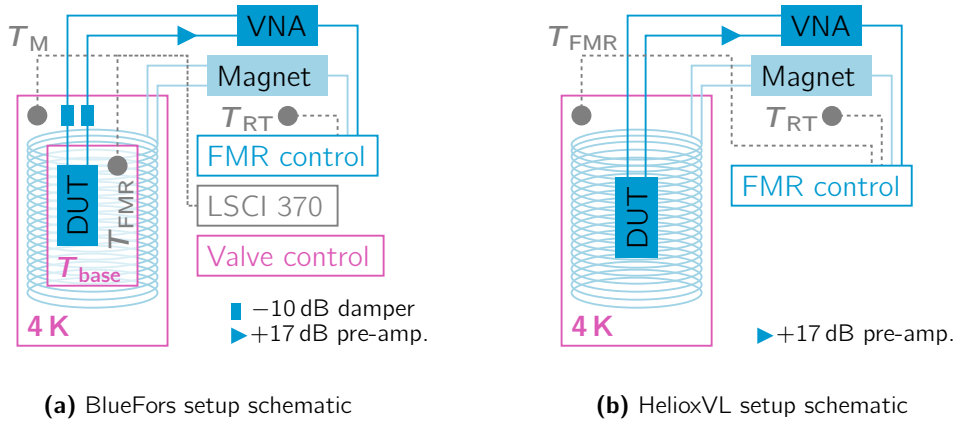
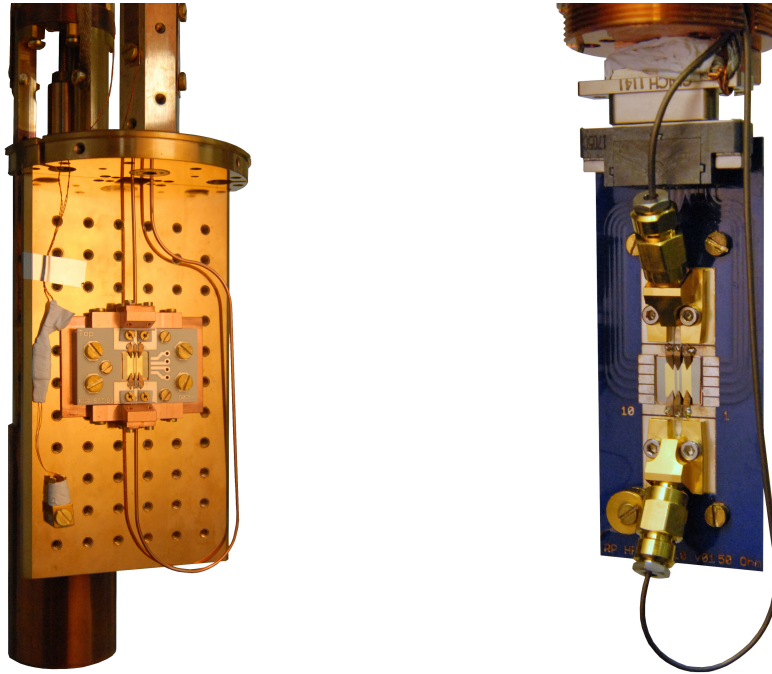


Figure 6 Schematics of the two used setups. In the magenta boxes the temperature can be set, to the indicated **4 K** or T_{base} . The grey full circles are indicating the thermometers, which are measuring T_{FMR} , T_M & T_{RT} . The blue color indicates the high-frequency part. It contains the device under testing (DUT), dampers, a pre-amplifier and the vector network analyzer (VNA). The light blue color indicates the magnet coils and its controller. In addition the three programs 'FMR control', 'LSCI 370' and 'Valve control' are connected to the corresponding devices.

Table 1 Devices used at BlueFors or HelioxVL setup

BlueFors	'BF-LD400' by 'BlueFors Oy' [38] stable temperature points: 4 K, $\approx 95 \text{ mK}$ (specified: 8 mK)
magnet	'AM430' by 'American Magnetics, Inc.' [39] $H_{\max} = 7 \text{ T}$, $\Delta H = 0.5 \text{ mT}$
thermometer	'LakeShore 370AC' by 'Lake Shore Cryotronics' [40] (incl. channel scanner 'LakeShore Model 3716') T_{FMR} range: 10 mK to 100 K ('RX-102B-CB') [41] T_{magnet} range: 4 K to RT (built-in)
HelioxVL	'HelioxVL' by 'Oxford Instruments' [42] stable at: 4 K, $\approx 300 \text{ mK}$
magnet	'IPS120-10' by 'Oxford Instruments' [43] $H_{\max} = 12 \text{ T}$, $\Delta H = 1 \text{ mT}$
thermometer	'LakeShore 370AC' by 'Lake Shore Cryotronics' [40] T_{FMR} range: 300 mK to RT ('CX-1010') [44]
VNA	'R&S® ZNB40, variant 82' by 'R&S GmbH & Co. KG' [45, 46, 47] f range: 100 kHz to 40 GHz P_{out} range: -5 to -30 dB P_{in} range: 25 to -140 dB
pre-amplifier	'U7227F/8C' by 'Keysight Technologies' [48] $P_{\text{gain}} = +17 \text{ dB}$
thermometer	'GIR 2002' by 'Greisinger electronic GmbH' [49, 50] T_{RT} range: -200 C° to 1350 C° (thermocouple, type K)



(a) BlueFors setup sample holder

(b) HelioxVL setup sample holder

Figure 7 Sample holder pictures. **(a)** shows the FMR sample holder, with the mechanically controlled break junction setup in the background. Sample CPW3 is mounted. On the left side of the plate, the thermometer for T_{FMR} is installed. **(b)** shows the sample holder of the Heliox setup. Beside the wave guide clamps, there are also bonding pads for direct current measurements. Again in the lower left, you can see the thermometer T_{FMR} without any cables connected.

HelioxVL Setup are controlled by the self-written program 'FMR control'. It is written in python3 and is mainly based on the packages pyvisa, numpy and matplotlib. It consists out of self-written device drivers and one central control program. By those drivers, the user can communicate with and control the devices. Several security features are implemented in them as well. Some device drivers can be found in the Appendix.

The measurement itself is run as multi-threading program, since recording the temperature, VNA and magnet control have to be done simultaneous. In general, at least one thread is recording the temperature the whole time. The logged temperature is averaged and then updated in a text file with corresponding timestamp. Another thread is controlling the magnet and VNA iteratively. Each iteration conducts the following operations. First, the magnet ramps to the desired field. Then the VNA measures the scattering parameter for all desired frequencies. A text file with the magnetic field, a timestamp and all the scattering parameter values and frequencies are saved. Afterwards these operations are conducted for the next desired magnetic field.

4 Technical Findings

At the beginning of this Chapter I want to clarify which quantities are measured. Then I will explain how the used measurement method works and how the signal processing is performed. After that I present what I did to optimize the signal. Later I will show what effect the ambient temperature has on the measurement. Further, I want to present the application of frequency domain reflectometry to find defects in the cabling. Finally, I will discuss the sample temperature dependence of the transmission.

Now we want to understand the measuring quantities of the vector network analyzer (VNA). It has two ports $i, j \in \{1, 2\}$. Therefore, one can measure four so-called scattering parameters S_{ij} , which are connecting the incident¹ wave amplitudes a with the outgoing wave amplitudes b , by

$$\begin{pmatrix} b_1 \\ b_2 \end{pmatrix} = \begin{pmatrix} S_{11} & S_{12} \\ S_{21} & S_{22} \end{pmatrix} \cdot \begin{pmatrix} a_1 \\ a_2 \end{pmatrix}. \quad (4.1)$$

In general, we are interested in the transmission. Therefore, we will concentrate further in the forward transmission scattering parameter, defined by

$$S_{21} = \frac{b_2}{a_1} = |S_{21}| e^{i\phi_{21}}. \quad (4.2)$$

Since we compare two wave amplitudes we can calculate the respective maximum amplitude $|S_{21}|$ and the phase difference ϕ_{21} as well.

When we want to do further calculus we always have to keep in mind that S_{21} is complex. So the absolute value and phase are given by

$$|S_{21}| = \sqrt{\operatorname{Re}(S_{21})^2 + \operatorname{Im}(S_{21})^2} \quad (4.3)$$

$$\phi_{21} = \operatorname{atan2}(\operatorname{Re}(S_{21}), \operatorname{Im}(S_{21})). \quad (4.4)$$

The `atan2` operator is an extension of the inverse angle function `atan`. If two Cartesian coordinates are passed as arguments to the `atan2` operator, the polar angle which is located in the correct quadrant is obtained. In consequence, the phase is given in a range of values from 0 to 2π .

When it comes to visualizing the scattering parameter, we will usually choose to plot the forward transmission T_{21} in decibel (dB). It is calculated by

$$T_{21} = 10 \cdot \log_{10}(|S_{21}|^2) = 20 \cdot \log_{10}(|S_{21}|). \quad (4.5)$$

In the following, I am interested in the transmission depending on the angular frequency ω and magnetic field H . Since it is more convenient in technical applications to use the frequency f with dimension Hertz (Hz), henceforth I will use $\omega/2\pi$, with dimension Hz². Likewise it is more convenient in technical applications, to express the magnetic flux density of a magnet in Tesla (T). Therefore, I will express the magnetic field H in terms of $\mu_0 H$, with unit T. [45]

¹Commonly the outgoing and incident waves are defined in respect to the device under test. So a is the output of the VNA, whereas b is the measured wave amplitude at the VNA.

²Since the typical frequencies are in the gigahertz regime, I will use GHz as unit.

4.1 Data Processing

Now we want to understand how the measured scattering parameter is related to the susceptibility and how we can make the ferromagnetic resonance (FMR) observable.

First, we consider the raw measured scattering parameter S_{21} as voltage ratio

$$S_{21} = \frac{V_{\text{sys}} + V_{\text{ind}}}{V_0}. \quad (4.6)$$

The voltage in the denominator V_0 is applied by the VNA, whereas the voltage in the numerator is a superposition of a systematic voltage V_{sys} and of a CPW induced voltage V_{ind} . The induced voltage is given by

$$V_{\text{ind}} = i\omega A \cdot V_0 \cdot \chi(\omega, H), \quad (4.7)$$

where A is a real-valued scaling parameter, that is dependent on the geometric dimensions of the co-planar waveguide (CPW) and the impedance of the entire system.

The systematic voltage is caused by the dielectric properties of the setup and depends only on the frequency. However, this voltage is much larger than the induced voltage. Since the FMR only affects the induced voltage, we have to consider it in the absence of the systematic voltage. That can be achieved by normalizing the measurement data by the normalization scattering parameter

$$S_{21}^0 = \frac{V_{\text{sys}}}{V_0}. \quad (4.8)$$

With that in mind, we can write the normalized scattering parameter as

$$S_{21}^n = \frac{S_{21}}{S_{21}^0} = 1 + \frac{V_{\text{ind}}}{V_{\text{sys}}} \approx 1 + \frac{V_{\text{ind}}}{V_0}. \quad (4.9)$$

Considering the induced voltage is way smaller than the voltage applied by the VNA $V_{\text{ind}} \ll V_0$ we can approximate $V_{\text{ind}}/V_{\text{sys}} \approx V_{\text{ind}}/V_0$.

Finally, our normalized scattering parameter is related to the susceptibility by

$$S_{21}^n = 1 + i\omega A \cdot \chi(\omega, H). \quad (4.10)$$

Thus, the normalized scattering parameter no longer depends on the systematic voltage V_{sys} or the voltage V_0 applied by the VNA. [51]

Now that we understand how we relate the normalized scattering parameter to the susceptibility, we can address the signature of the FMR signal. From Chapter 2.2 we already know that the FMR frequency for an in-plane magnetized film is finite even in the absence of an external magnetic field. For applied fields the FMR frequency increases continuously. If negative fields are included, an axial symmetry to the zero-field line results. This leads to a typical curved Y-shape around the zero-field line, which becomes straighter for higher fields. The transmission decreases in the presence of the FMR.

The simplest method to determine the normalization scattering parameter is to find a frequency curve at a fixed magnetic field, which does not carry a FMR signal with certainty. Therefore, the maximum measured magnetic field H_n , where the FMR frequency is out of the measurement range is usually used for normalization. The normalization scattering parameter S_{21}^0 is then given by

$$S_{21}^0(\omega) = S_{21}(\omega, H_n). \quad (4.11)$$

The normalized scattering parameter S_{21}^n and the normalized transmission T_{21}^n are calculated by³

$$S_{21}^n = S_{21}(\omega, H) / S_{21}^0(\omega), \quad (4.12)$$

$$T_{21}^n = T_{21}(\omega, H) - T_{21}^0(\omega). \quad (4.13)$$

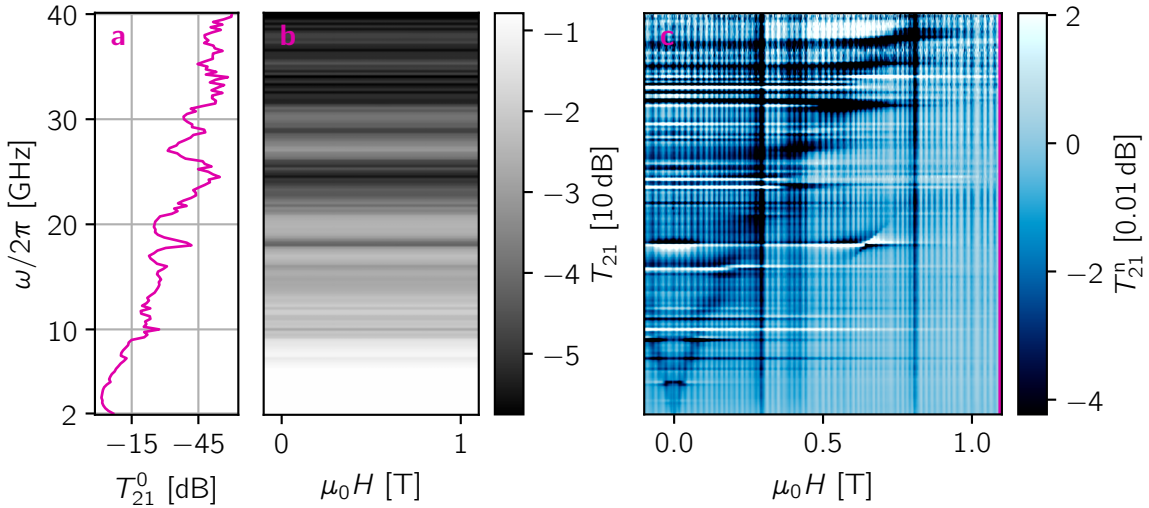


Figure 8 Transmission T_{21} of sample CPW2 depending on the frequency $\omega/2\pi$ and magnetic field $\mu_0 H$. In **a**, you can see the transmission T_{21}^0 for a fixed field at $H_n = 1.1$ T. In **b** you can see a colorless grey scale map of the raw transmission T_{21} . In **c** you can see a false color map of the normalized transmission T_{21}^n .

Figure 8 shows data obtained of sample CPW2 as an example for the normalization of the transmission. In panel a you can find the normalization transmission T_{21}^0 , in panel b the raw transmission T_{21} and in panel c the normalized transmission T_{21}^n . The Y-shaped FMR signal is clearly observable and not present at maximum field. At this point, I would like to emphasize the large amplitude ratio between raw and normalized transmission. The data range of the raw transmission covers approximately 60 dB, whereas the normalized transmission covers a data range of approximately 0.06 dB.

Now we want to turn to the quantitative evaluation of the FMR. In the following, I present an algorithm that provides reliable minima in the normalized transmission despite strong noise. The algorithm was applied to measurements of samples CPW2 and CPW3 and is visualized in Figure 9. First, I uniformly resized the datasets to a window from 0 to 1 T and reduced the magnetic field resolution from 0.5 mT steps to 5 mT steps by averaging. Dataset CPW3 was cut off below 5 GHz, because there is no signal. Additionally, for this dataset, the frequency resolution was reduced from 20 MHz to 250 MHz by averaging. Now both datasets have the same resolution in frequency and magnetic field direction. Also the considered magnetic field section and the maximum frequency is the same. By averaging, some noise could already be reduced.

The normalized transmission T_{21}^n is calculated as before using the normalization transmission T_{21}^0 at $H_n = 1$ T. Then I additionally normalize the transmission line-by-line to a range from 0 to 1 in arbitrary units⁴. Further, I form the median row-by-row $\langle \tilde{T}_{21}^n(\omega) \rangle_H$ and subtract it from each row. These additional normalizations allow an effective reduction of frequency dependent noise. In magnetic field direction already subtracting the column-wise formed median $\langle \tilde{T}_{21}^n(H) \rangle_\omega$ achieves a sufficiently good reduction of magnetic field noise. Then I mask frequency bands that are still highly noisy. Additionally, I mask data that are far away from the visible FMR signal.

Now minima are determined row-by-row and column-by-column. Its advantage is that many minima are obtained. The disadvantage is that some minima are lined up vertically or horizontally. Nevertheless, to prevent excessive weighting for horizontal or vertical features, I join the minima row-by-row and column-by-column. This means, e.g. that several minima obtained row-by-row at the same magnetic field are reduced to one minimum by averaging. The magnetization properties, which can be determined from the obtained minima, are discussed in Chapter 5.

³Always keep in mind, that algebraic operations looks different for T_{21} than for S_{21} , since they are logarithmic quantities.

⁴Since I am not working with quantitatively comparable transmissions, I use again \tilde{T}_{21}^n as notation

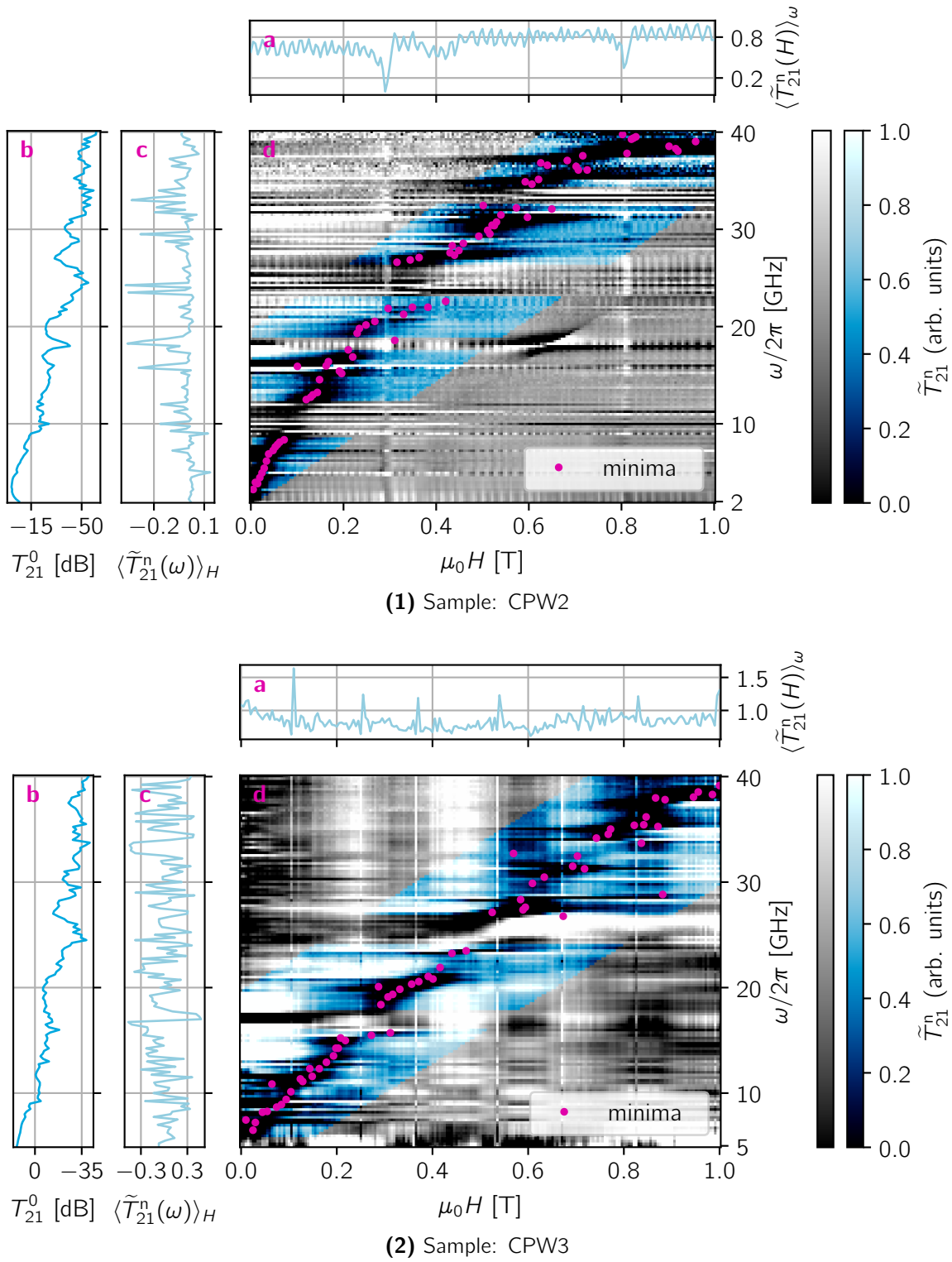


Figure 9 Normalized transmission and minima as a function of frequency $\omega/2\pi$ and magnetic field $\mu_0 H$. The measurement of sample CPW2 is shown in **(1)** and of sample CPW3 is shown in **(2)**. Normalized transmission (false color) and minima found (**magenta**) are shown in **d**. Masked data areas are decolorized. In **b**, the normalization transmission T_{21}^0 in **blue** for $H_n = 1$ T can be seen. In **a** and **c**, the determined median curves $\langle \tilde{T}_{21}^n(\omega) \rangle_H$ and $\langle \tilde{T}_{21}^n(H) \rangle_\omega$ are plotted in **light blue**.

4.2 Modeling

In this Section I will take the opportunity to present several other background treating methods, even though they did not yield better results than the already described method.

In another approach, instead of a fixed-field reference, as used in Section 4.1, a moving-field reference is used. We consider a small frame around the theoretically predicted resonance frequency $\omega_{\text{res}}^{\text{theo}}(H)$, with width $\Delta\omega_f$. So, we evaluate the scattering parameter solely in this field, given by

$$S_{21}^f = S_{21}(\omega_{\text{res}}^{\text{theo}}(H) \pm \Delta\omega_f, H). \quad (4.14)$$

As in Section 4.1 discussed, I took the highest field within the given frame to obtain a reference curve. The normalization scattering parameter is given by

$$S_{21}^{f,0} = S_{21}(\omega, H_n). \quad (4.15)$$

The normalized scattering parameter is calculated as before by

$$S_{21}^{f,n} = S_{21}^f / S_{21}^{f,0}. \quad (4.16)$$

You can see an example for the moving-field reference in Figure 10.3, right next to a fixed-field reference background treatment in Figure 10.1. [33, 52]

In comparison to the fixed-field method, the moving-field reference method has a slight advantage when it comes to line-by-line averaging. The drifts within one line are not that pronounced in comparison to the fixed-field normalization. You can see an example for line-by-line averaging in Figure 20, in the Appendix. Due to the complexity of calculating the moving-field this method is not used further.

Next, I want to present the so-called 'derivative divide' method by Hannes Maier-Flaig [32, 33]. This method is particularly suitable for out-of-plane measurements, because then the FMR signal is strictly linear as function of the magnetic field. Even if this is true for high magnetic fields and in the in-plane case, this is not the case for smaller magnetic fields. Therefore, the application is not quite suitable, even though the method removes interfering temperature drifts and frequency dependencies without prior system calibration. The basic idea is to calculate the numerical deviation of the scattering parameter by

$$d_D S_{21} = \frac{S_{21}(\omega, H + \Delta H_{\pm}) - S_{21}(\omega, H - \Delta H_{\pm})}{S_{21}(\omega, H) \cdot \Delta H_{\pm}}, \quad (4.17)$$

where ΔH_{\pm} is the step width. We can easily show that $d_D S_{21} = d_D S_{21}^n$ holds true. Therefore, it makes no difference whether the raw or normalized scattering parameter is used to calculate the numerical derivative.

However, the deviated scattering parameter is related to the susceptibility by

$$d_D S_{21} = i\omega A' \frac{\chi(\omega + \Delta\omega_{\pm}) - \chi(\omega - \Delta\omega_{\pm})}{2\Delta\omega_{\pm}}, \quad (4.18)$$

where $\Delta\omega_{\pm}$ is the frequency step, given by approximately $\Delta\omega_{\pm} \approx \gamma\mu_0\Delta H_{\pm}$. You can find an application example in Figure 10.2. In advance the resolution of the data was strongly reduced by averaging in order to achieve the best visible results.

Finally, there is also the uncalibrated effective microwave permeability parameter

$$U(\omega) = \pm i \frac{\ln(S_{21}^n(\omega, H))}{\ln(S_{21}^0(\omega, H))}. \quad (4.19)$$

The sign is chosen in the way, that $\text{Im}(U(\omega))$ is negative in the vicinity of the FMR peak. [16, 53]

The susceptibility can be fitted by

$$U_{\text{fit}}(\omega) = C \left(1 + \chi_0 + \chi(\omega) e^{i\phi} \right), \quad (4.20)$$

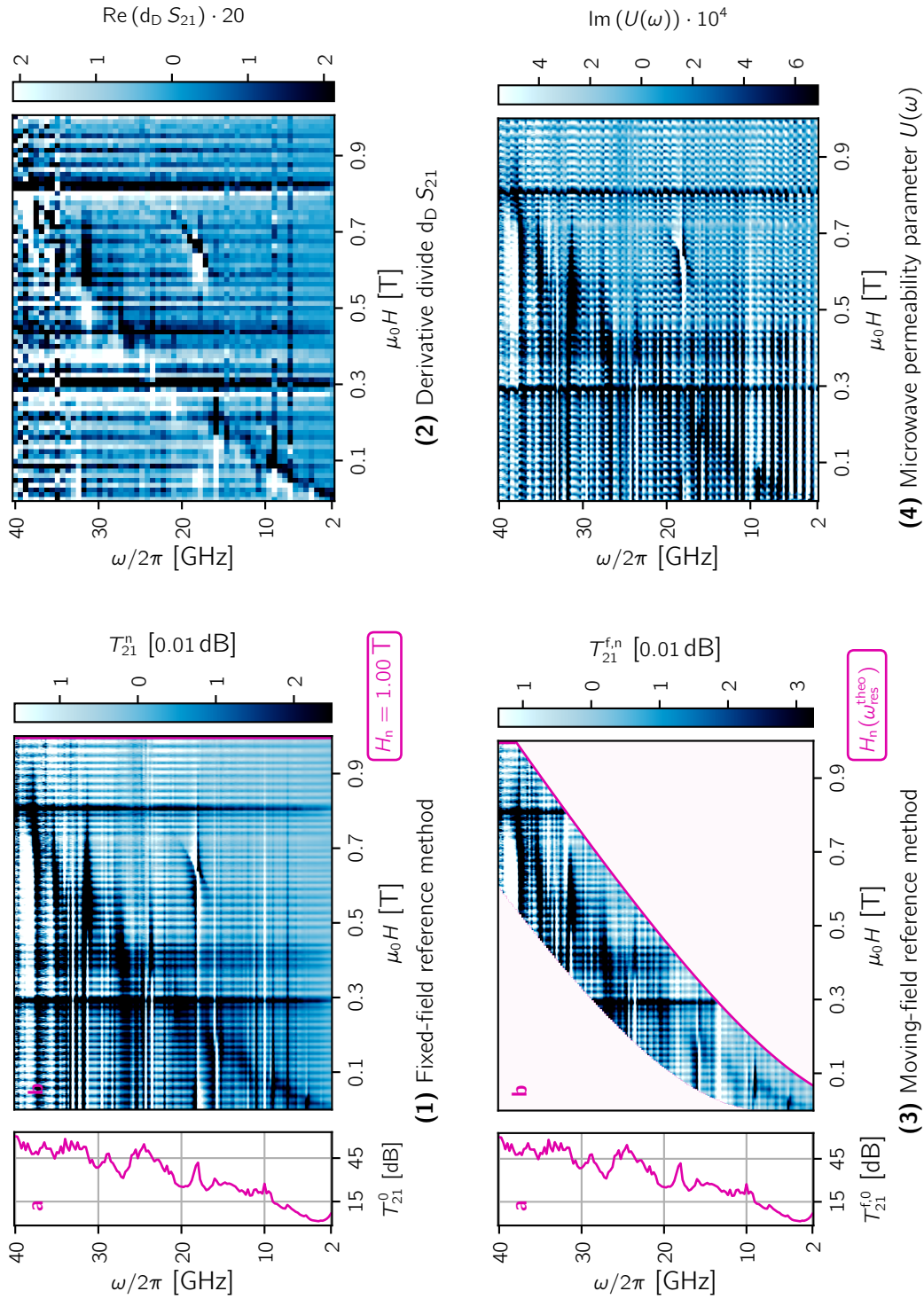


Figure 10 Comparison between different signal enhancement methods for transmission data of sample CPW2, depending on the frequency $\omega/2\pi$ and the magnetic field $\mu_0 H$. In (1) and (3) the two normalization methods fixed-field reference and moving-field reference are shown. In **a** the normalization transmission is shown and in **b** the normalized transmission. Additionally, the course of the magnetic field H_n selected for normalization is shown in magenta. (2) shows the real part of the derived scattering parameter $\text{Re}(d_D S_{21})$. (4) shows the imaginary part of the microwave permeability parameter $U(\omega)$.

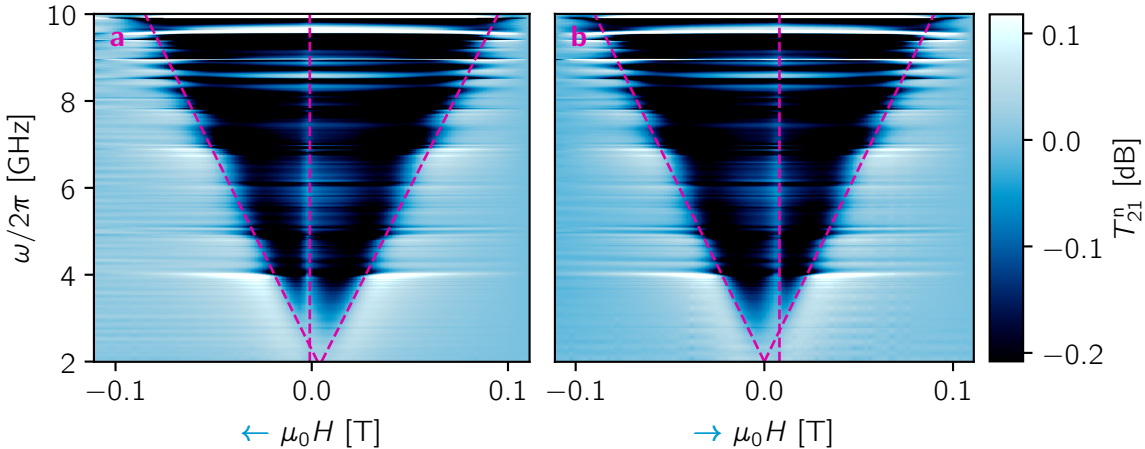


Figure 11 Normalized transmission T_{21}^n in down (\leftarrow , **a**) and up (\rightarrow , **b**) sweep direction in dependence of frequency $\omega/2\pi$ and magnetic field $\mu_0 H$ of CPW1 measured at the HelioxVL setup, initially magnetized at 3 T. In addition, dashed lines in **magenta** have been added for visual emphasis.

where C is a real-valued scaling parameter, χ_0 is a complex offset and ϕ is a phase shift. You can see an application example in Figure 10.4. [32, 33]

All these modeling approaches try to reduce background noise, depending on the frequency, but also apparently on the field. It is quite obvious that there is still significant noise left in the data. Therefore, I will discuss further signal optimization in the next Section and the obtained magnetization properties in Chapter 5.

4.3 Signal Optimization

In this Section I would like to present chronologically various results of my work that have a strong technical aspect and deal with signal optimization. First, I will start with the HelioxVL setup and present my findings on the hysteresis of the setup. Then the results obtained by this setup and the BlueFors setup will be compared. Afterwards, datasets that were recorded either in the frequency direction or in the magnetic field direction will be compared. Finally, the parameters I used will be discussed and recommendations for future measurements will be given.

4.3.1 HelioxVL Setup Magnetization

To gain a better understanding of the signals obtained in the HelioxVL setup, I performed several initial measurements. To this end, I performed fast, low-resolution measurements on sample CPW1. Another aspect of these studies addresses the role of the field sweep directions and their possible advantages.

The results with the FMR typical Y-shape can be examined in Figure 11. After a +3 T initialization I started the measurement first at +320 mT (down sweep, \leftarrow , panel a) and then at -320 mT (up sweep, \rightarrow , panel b).

It is easy to see that the center of the Y-shaped FMR signal is shifted by +4 mT towards zero in the down sweep, whereas in the up sweep the Y-shape is exactly occurring at 0 mT. It is conceivable that the magnet has a small offset, but as well that components of the cryostat can be magnetized. A frequency independent feature can be observed in both measurements. In the case of the up sweep, it is at +8 mT and in the down sweep at -1 mT. What is the cause of this feature has not been investigated further. However, this also speaks for a hysteretic magnetization effect. We were able to determine that the SK connector of the measurement line are ferromagnetic and are very likely responsible for this hysteretic magnetization.

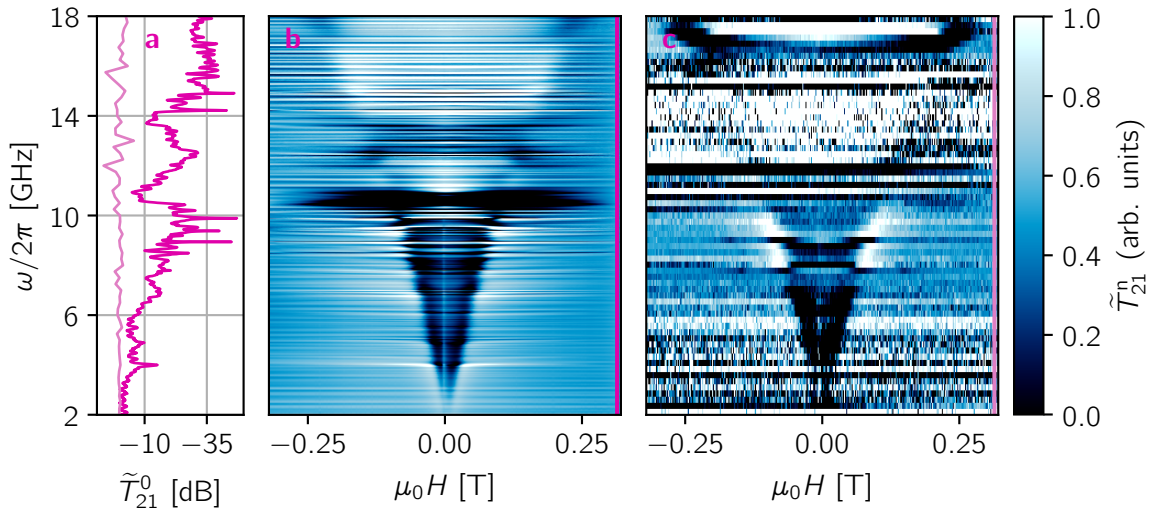


Figure 12 Normalized transmission \tilde{T}_{21}^n of the same sample CPW1 in the setups HelioxVL (**b**) and BlueFors (**c**) in dependence of frequency $\omega/2\pi$ and magnetic field $\mu_0 H$. In panel **a** the normalization transmissions \tilde{T}_{21}^0 in **magenta** and **light magenta** at $H_n = 315$ mT are shown.

For future measurements initialization has been omitted, as I have also measured with way stronger magnetic fields. I assume that magnetic fields around 1 T are sufficient to neglect any magnet training effects. So, inherent down sweeps from the initially applied magnetic field are measured. Of course this can still be varied in sign.

4.3.2 Comparison of the Setups Used

Finally, one focus of my work was to reproduce the FMR measurements in the HelioxVL setup. This measurements were already done previously in the BlueFors setup by Sergej Andreev. To this end, I wanted to use a sample with the strongest potential signal. Since this depends on the volume, I used CPW1 already described in Section 3.1.

Even though both measurements use very different measurement parameters and different sweep types, they can be compared qualitatively. The measurement at the BlueFors was done with Sergej Andreev's measurement program. This measurement method is explained in detail in Section 4.3.3.

Panel a of Figure 12 shows the normalization transmissions, obtained at a magnetic field $H_n = 315$ mT. In magenta, the raw transmission measured in the HelioxVL setup and in light magenta, the already zero-field calibrated transmission measured in the BlueFors setup is shown. The normalized transmission measured in the HelioxVL and BlueFors setup is shown in panel b and c.

Even though both measurements are different in noise shape and noise intensity due to the different parameter and sweep types, the Y-shape typical for FMR is recognizable. Despite all this, it can be said with certainty that FMR measurements can be made on both setups.

4.3.3 Magnetic Field and Frequency Sweep method

Usually, the VNA measures the scattering parameters for all set frequencies in a single sweep⁵. Therefore, it seems only natural to set a fixed magnetic field and then measure a frequency sweep. In the following, I will refer to this procedure as frequency sweep method.

However, also with a fixed frequency, the magnetic field can be swept. Henceforth, I will call this method the magnetic field sweep method. This method was previously implemented by Sergej Andreev and measured with his measuring program.

⁵Even though this is called a sweep, the VNA measures per default in a so called stepped method. Here each frequency is set before measurement and is changed just after the measurement. [45]

The measurement procedure of the magnetic field sweep method differs from the frequency sweep method in that a zero-field calibration is carried out first. At this point, the magnet is given a sweep rate and target. As the magnetic field changes continuously, the VNA measures miniate frequency sweeps, with a small span around a center frequency. The collected data, magnetic field, frequency, transmission and phase are then averaged to obtain a data point. For visualization, a binning algorithm is also used later, in which transmission and phase are averaged again.

A problem that should not be underestimated is the averaging. As I mentioned in the beginning, the transmission is a logarithmic quantity. Therefore the scattering parameter needs to be used to calculate a mean value instead and calculate the transmission from that, as

$$T_{21}(\overline{S_{21}}) = 20 \cdot \log_{10}(|\overline{S_{21}}|) \quad (4.21)$$

$$= 20 \cdot \log_{10}\left(\left|\frac{1}{N} \sum_{i=0}^N S_{21,i}\right|\right). \quad (4.22)$$

However, calculating the mean of the transmission directly, can be traced back to a geometric mean of the magnitude of the scattering parameter, like

$$\overline{T_{21}} = \overline{20 \cdot \log_{10}(|S_{21}|)} \quad (4.23)$$

$$= \frac{20}{N} \cdot \sum_{i=0}^N \log_{10}(|S_{21}|)_i; \quad (4.24)$$

$$= 20 \cdot \log_{10}\left(\prod_{i=0}^N \sqrt[N]{|S_{21}|_i}\right). \quad (4.25)$$

Fortunately, the transmission values within a miniate sweep and between neighbouring data points do not differ much. Considering this, the geometric mean and arithmetic mean are quite close to each other. Therefore, it is still possible to discuss semi-quantitatively. Larger differences can only be found, if there are strong outliers among the values, which is why the geometric mean is often used as a noise filter. I will use \tilde{T}_{21} when the geometrically and arithmetically averaged transmission values are compared. [54]

Superconducting magnets, as we use them, can only be swept very slowly. This results in a disadvantage of the magnetic field sweep method with respect to the measurement speed. Thus, at a constant frequency the field is swept up at maximum rate and then swept down again. During this process it is possible to measure well. However, there is no great information gain to measure up and down sweep each time.

In Figure 13 a comparison of two measured down sweeps is made between frequency sweep method (panel b) and with magnetic field sweep method (panel c). The up sweep dataset of the magnetic field sweep method is available, but does not provide any additional relevant information and is therefore not shown.

So, for each frequency a whole up and down sweep of the magnetic field has to be repeated. With limited measurement time the frequency resolution is therefore severely limited. Thus, in Figure 13c a frequency step size of 250 MHz can be seen, with a total measurement time of about 200 h.

With the frequency sweep method, on the other hand, there are more options regarding the parameters. A higher frequency resolution of 20 MHz is usually used. However, the two measurements seen in Figure 13 were made with the same parameters such as resolution and range. By repeatedly averaging the same frequency sweep at the same field, the frequency sweep method could be slowed down to a total measurement time of about 75 h for a down sweep dataset. With well comparable FMR signals between magnetic field sweep method and frequency sweep method the frequency sweep method is clearly faster.

Finally, I want to talk about another not that obvious advantage of the frequency sweep method. When it comes to noise apparently the frequency sweep measurement in Figure 13b has additional

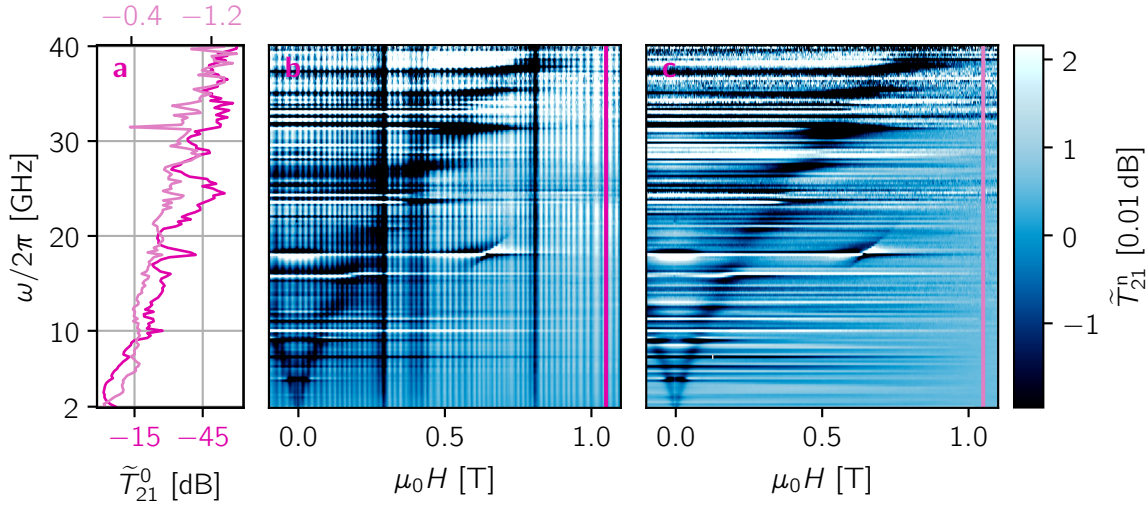


Figure 13 Normalized transmission \tilde{T}_{21}^n of the same sample CPW2 at the BlueFors setup in frequency sweep method (**a**) and magnetic field sweep method (**b**) in dependence of frequency $\omega/2\pi$ and magnetic field $\mu_0 H$. Panel **a** shows the normalization transmissions \tilde{T}_{21}^0 in **magenta** and **light magenta** at $H_n = 1.05$ T.

noise. In both measurements horizontal lines can be seen, most likely due to frequency depending effects. However, in the frequency sweep method additionally vertical lines appear. Since we can exclude magnetic dependencies by the magnetic field sweep measurement, we have to assume, that some time dependent noise is disturbing the measurement. This time-dependent noise is included in both measurements but can only be resolved separately from frequency-dependent noise in the frequency sweep method. In the next Section, this time-dependent noise will be explained in more detail.

4.3.4 Noise Induced by the Laboratory Temperature

In this Section I would like to talk about temperature induced noise. I could show that the room temperature in laboratory P10 varies up to 2 °C. This significantly disturbs the BlueFors measurement electronics, consisting of VNA and pre-amplifier.

Essentially, I made three measurements to show the laboratory temperature induced noise. The results of these measurements are shown in Figure 14.

For measurement one I connected the output and input of the VNA and measured the transmission for all set frequencies, shown in Figure 14a. For measurement two I connected the pre-amplifier in between, shown in Figure 14b. Measurement three is shown in Figure 14c and is made with a temperature stabilization⁶, to control the temperature of the pre-amplifier. Simultaneously, I logged either the room temperature T_{RT} , or the temperature within the styrofoam box T_{box} , used for isolation.

Besides a regular fluctuation of the room temperature in measurements one and two in a 0.5 to 1 h cycle, a particularly strong fluctuation occurs every 10 to 12 h. I guess this has to do with the air conditioning of the laboratory. Furthermore, a low frequent fluctuation with a period of 24 h can be observed. This means that the laboratory temperature depends slightly on the time of day. The high frequency fluctuations in measurement two are way more irregular in amplitude. This can be explained by the fact that the temperature is more stable at weekends (measurement one) compared to during the week (measurement two) with higher numbers of people in the laboratory.

⁶The stabilization consists out of a temperature controller and a styrofoam box for isolation. The temperature controller was built by Sergej Andreev and consists out of a Peltier element and a water cooling system. This setup can control the pre-amplifier to stable 25 °C.

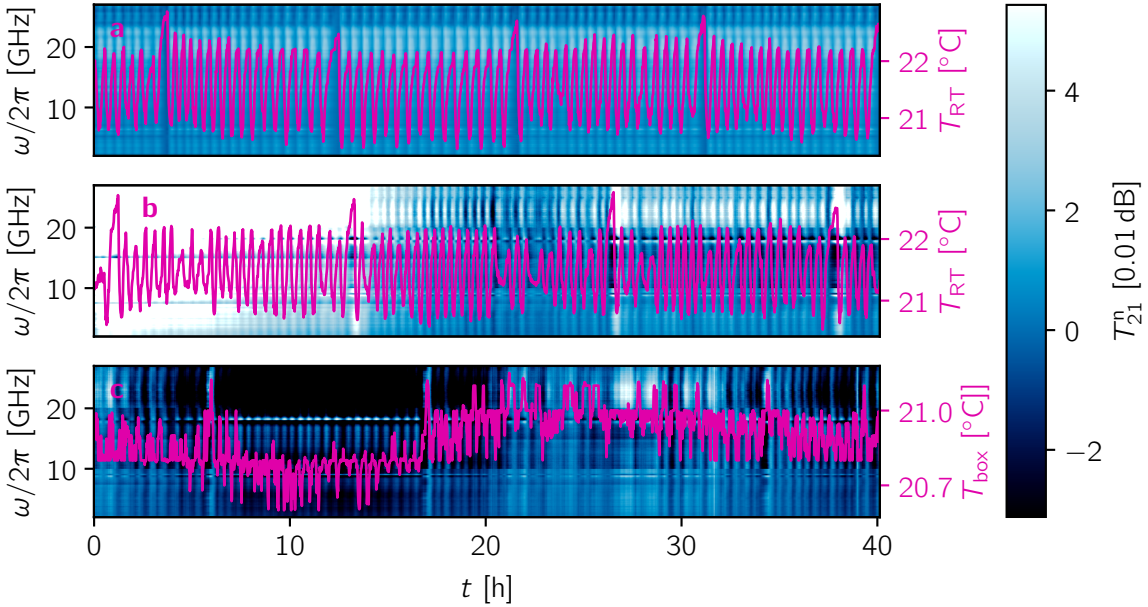


Figure 14 Normalized transmission T_{21}^n over frequency $\omega/2\pi$ and as well as temperature over time t . The temperature is either measured in the laboratory T_{RT} or the box T_{box} , used for isolation. For normalization the last transmission $T_{21}^0(t_{max})$ was used. **a**, **b** & **c** are showing the measurements without and with tempered pre-amplifier.

Measurement one without a pre-amplifier shows that the transmission varies together with the temperature. To compare the fluctuation quantitatively I calculated the average value column-by-column and then calculated the standard deviation σ (STD) of both the transmission and the temperature. The room temperature has a STD of $\sigma(T) = 0.53^\circ\text{C}$. The transmission has a STD of $\sigma(\langle T_{21} \rangle_\omega) = 3.9 \cdot 10^{-3}$ dB. Calculating the ratio of these we get $\sigma(\langle T_{21} \rangle_\omega)/\sigma(T) = 7.3 \cdot 10^{-3}$ dB/ $^\circ\text{C}$, which is even slightly better than the specified drift of 0.01 dB/ $^\circ\text{C}$ for the VNA. [47]

In measurements two and three, frequency bands with different temperature-dependent transmission characteristics appear. Especially in the higher-frequency third, temperature-dependent transmission fluctuations are clearly visible. Especially the day-dependent temperature fluctuations seem to have a strong effect on the transmission. The transmission in measurement two is significantly higher in the first ≈ 15 h. This can be explained by a self-induced heating-up of the pre-amplifier to a stable operating temperature.

Quantitatively, the STD of transmission in the whole measurement two is $\sigma(\langle T_{21} \rangle_\omega) = 4.7 \cdot 10^{-2}$ dB, in the second half of measurement two the STD is $\sigma(\langle T_{21} \rangle_\omega) = 1.3 \cdot 10^{-2}$ dB and in measurement three the STD is $\sigma(\langle T_{21} \rangle_\omega) = 1.6 \cdot 10^{-2}$ dB. It would be interesting to know how much the laboratory temperature varied during measurements three, since the transmission varies more than in the second half of measurement two. However, it can be deduced from the box temperature T_{box} that the cooling of the pre-amplifier works reliable. The temperature fluctuations are characterized by the course of the day, which suggests a cooling water temperature fluctuation.

Only from the transmission noise perspective the further use of the pre-amplifier is not recommended. Nevertheless, its usage is recommended especially at higher frequencies, since the signal gain of the pre-amplifier outweighs the higher noise. For comparison two measurements with and without tempered pre-amplifier are shown in Figure 21, in the Appendix.

4.3.5 Parameter Study

In this Section I would like to make recommendations for the parameter space to be chosen. Often enough, the measurement time is limited and cannot be increased arbitrarily. Here I mainly refer to the magnets, the VNA and the pre-amplifier used.

Magnetic fields can be adjusted in steps of down to 0.5 mT and I would also recommend working with that stepsize. For fast measurements you can also increase to 1 mT steps. From Section 4.3.1 we know that asymmetries can arise around 0 T, so measurements should also be made generously around 0 T. The maximum frequency used of the VNA is 40 GHz, with the gyromagnetic ratio of about 28 GHz/T, the upper FMR limit for nearly spherical geometries is about 1.4 T. In practice, it has turned out that only fields up to 1.1 T are interesting, since in-plane measurements are conducted. Summarizing, I would recommend a measurement between -50 mT and 1.2 T in 0.5 mT steps, which corresponds to 2501 measuring points in magnetic field direction. [39, 43]

The VNA provides a frequency range from 100 kHz to 40 GHz, which in general I would always use. For faster measurements the frequency can be cut off below the upper limit. Thus, the signal strength for high frequencies also decreases strongly, e.g. in Section 4.3.4, I only measured up to 26 GHz. In combination with the pre-amplifier measurements should only be taken from 2 GHz, as this only supports frequencies between 2 to 50 GHz. The number of measurement points is almost arbitrary⁷. Therefore, the increase in total measurement time has to be considered. In practice around 2000 points have proven to be useful. I would suggest measurements between 2 GHz and 40 GHz, in 20 MHz steps. That corresponds to 1901 measuring points in frequency direction. [45, 48]

With an image resolution of 2501×1901 points, it is easy to zoom into features afterwards. Also, a smoother image can be achieved by averaging afterwards.

Unfortunately, no reliable numbers on the relationship between bandwidth and dynamic range can be found in the VNA specifications. However, it is certain that the smaller the bandwidth, the better the resolution for small signal strengths. However, with a smaller bandwidth the measurement time increases. Averaging over several frequency sweeps helps as well against noise, which also increases the measurement time. While in the end it is always a question of weighing measuring time against signal strength, in practice, it has been shown that a bandwidth of 1 kHz and 10 averages yields satisfying results, when the pre-amplifier is used. If you want to measure without a pre-amplifier, a bandwidth of about 30 Hz and 3 averages is recommended. In general, the use of the pre-amplifier is recommended, especially for frequencies above 30 GHz. [45, 47, 46]

4.4 Frequency Domain Reflectometry

Frequency domain reflectometry (FDR) is a commercially available, powerful software for analyzing transmission lines with a VNA. I utilized the measured reflection scattering parameters to find wiggle contacts by applying a fast Fourier transform myself. Since this technique was implemented by Smith-Rose in the 1930s, more sophisticated reconstruction algorithms have been put forward. Because a limited understanding of this technique will suffice in the following, I will not go into detail. More information can be found following sources, [55, 56, 57, 58].

The reflection scattering parameter $S_{ii}, i \in \{1, 2\}$ is defined by

$$S_{ii} = \frac{b_i}{a_i}. \quad (4.26)$$

The VNA measures the scattering parameter as a function of frequency. From frequency domain to the time domain can be switched by applying the symmetrized ortho-normalized fast Fourier

⁷Technically it is limited to 100001 points by the VNA. However, you can split your sweep into several sub-sweeps. Doing so the number of points can increase significantly.

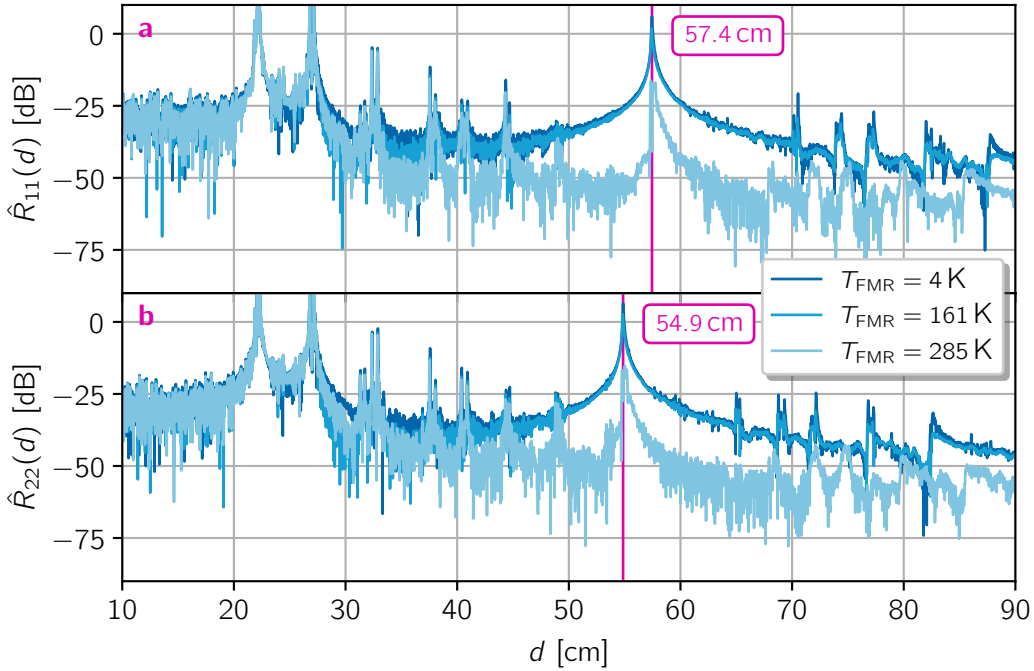


Figure 15 Reflection parameters \hat{R}_{11} & \hat{R}_{22} in panel **a** & **b** as a function of resonator length d . Three measurements each at **4 K**, **161 K** and **285 K** are shown. The maximum of the dominant wide peaks are marked in **magenta** at 57.4 cm and 54.9 cm.

transformation

$$\hat{S}_{ii}(t) = \text{FFT} (S_{ii}(f)) . \quad (4.27)$$

Now I rescale the time-axis to get the typical resonator length d , by

$$\Delta d = \frac{c_0 / \sqrt{\epsilon_r}}{2 \cdot 2\pi \Delta f} . \quad (4.28)$$

Here is c_0 the speed of light and the factor of propagation velocity can be approximated as $1/\sqrt{\epsilon_r} \approx 0.70 - 0.77$ for common microwave cables, where ϵ_r is the relative permittivity. A factor of 2 is inserted, on account of the typical resonator length and not the path length is to be considered. [59, 60]

Finally, the reflection parameter in decibels is calculated by

$$\hat{R}_{ii}(d) = 20 \cdot \log_{10} (|\hat{S}_{ii}(d)|) . \quad (4.29)$$

In the following, I will use an example to explain the possibility of finding a loose contact in the transmission line. The transmission has drastically decreased in the course of a cooling process. I have carried out three reflection measurements during the warm-up process.

The first measurement was made at 4 K, the second at 161 K. The high temperature superconducting cables used in some sections are superconducting only up to about 75 K, see next Section 4.5. The transmission during the first two measurements were significantly worse than I would usually expect and leads me to the conclusion that the transmission line is interrupted. The last measurement was taken near room temperature at 285 K. At this temperature I was able to measure the expected transmission and I can assume that the transmission line is intact again.

The respective reflection parameters \hat{R}_{11} & \hat{R}_{22} as a function of resonator length d can be seen in Figure 15. The reflection parameters at 4 K and 161 K did not differ significantly from each other in their magnitudes and are referred as interrupted state in the following. The reflection parameters at 285 K in intact state differs significantly from the other reflection parameters measured.

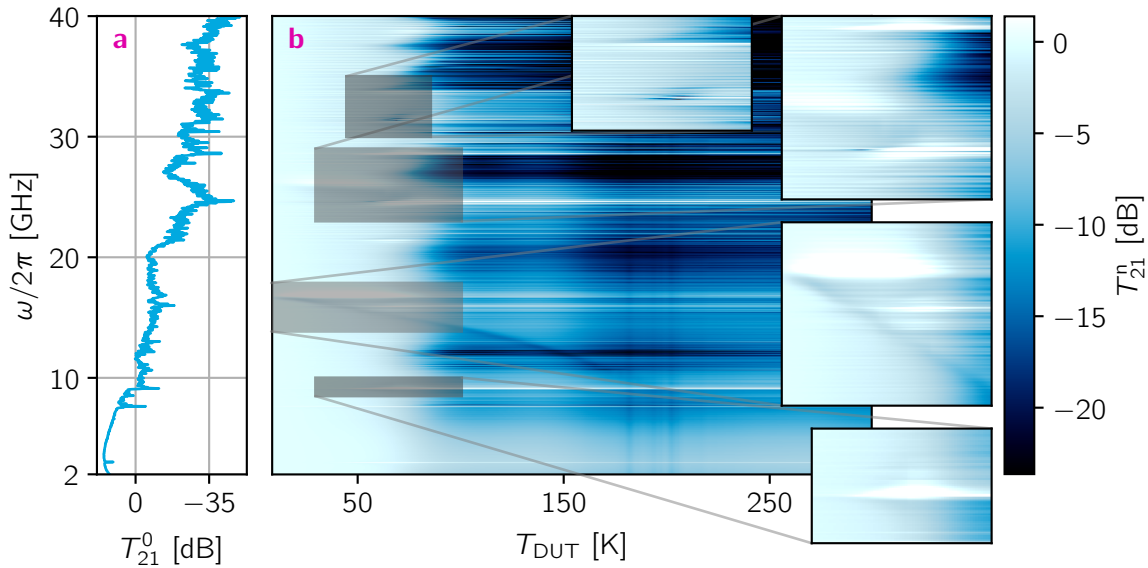


Figure 16 Transmission behavior of sample CPW3 over temperature T_{DUT} during warm-up process. In panel **a** you can see the normalization transmission at 7 K. In panel **b** the normalized transmission T_{21}^n over the complete temperature range is shown. Four insets for close-ups are included as well.

The first two strong peaks are formed at resonator lengths corresponding to the distance between the -10 dB dampers of the setup and the adjacent connectors. The second peak, like most of the following peaks, looks like double peaks. This can be explained by the placeholders that are built in instead of the original dampers. The placeholders and the next cable termination form two resonators of only slightly different length. The following peaks corresponding to resonator length up to 50 cm can all be explained by resonances in the different cable parts.

Around a resonator length of 57.4 cm, respectively 54.9 cm a broad peak builds up in the interrupted state measurements. This resonator length corresponds to the cable Sections between the sample holder and the mixing chamber (MXC). There is a significant difference in magnitude between the interrupted and intact state of the cables. From this difference I conclude that the interruption of the transmission line must be at the cable connection to the PCB⁸. However, even in the intact state, the peaks corresponding to the same resonator length, are still higher than most of the peaks corresponding to smaller lengths. This is again to be expected since the inner conductors of the cable are simply pressed onto a PCB board in the sample holder, thus a higher reflection is assumed than within a commercial connector. I attribute the peaks at higher resonator lengths, to higher resonance orders.

In summary, I could show that with the measurement of both reflection scattering parameters in interrupted and intact state, a localization of a interruption in the transmission line is possible just by using the VNA.

4.5 Transmission Dependency on Sample Temperature

Since I measured at low temperatures, between 50 mK and 4 K, I am also interested in changes of the transmission over the temperature. For this reason, I constantly logged the transmission and temperature of sample CPW3 during a warm-up process. The results can be seen in Figure 16.

Since the thermometer of the sample holder (T_{FMR}) is not calibrated up to room temperature, in comparison to the magnet thermometer (T_{magnet}), the device under test (DUT) temperature

⁸The inner conductor pressed onto the PCB board was stripped too tightly and pulled off the PCB board when it cooled down. I was able to fix this by stripping the inner conductor again generously.

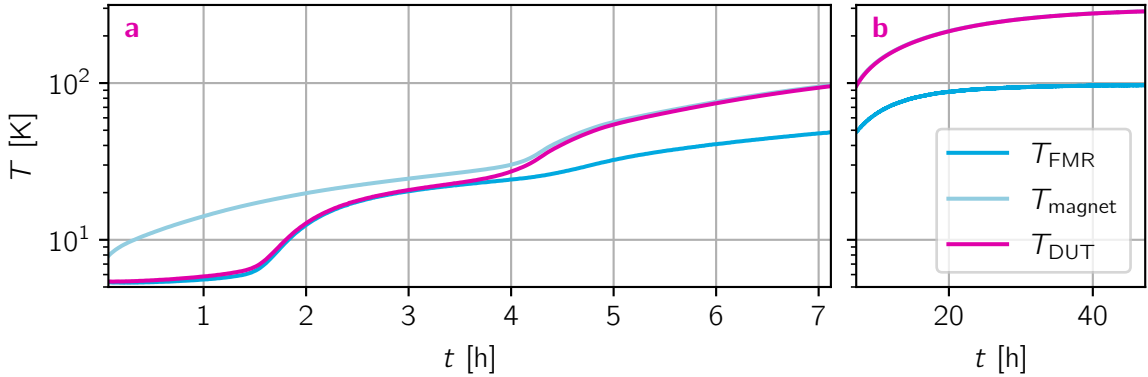


Figure 17 Typical warm up curve over time of the BlueFors setup. T_{FMR} & T_{magnet} are measured temperatures, whereas T_{DUT} is calculated by those temperatures and some atan weights. Panels **a** & **b** are showing different time periods. The parameters are $t_0 \approx 4$ h and $\Delta t \approx 20$ min

T_{DUT} was calculated by

$$T_{\text{DUT}}(t) = \left(\frac{1}{2} + \text{atan} \left(\frac{t - t_0}{\Delta t} \right) \right) \cdot T_{\text{FMR}}(t) + \left(\frac{1}{2} - \text{atan} \left(\frac{t - t_0}{\Delta t} \right) \right) \cdot T_{\text{magnet}}(t). \quad (4.30)$$

The parameters t_0 and Δt were chosen so that when the two measured temperatures begin to diverge at about 25 – 30 K, T_{DUT} begins to converge from T_{FMR} to T_{magnet} . This was visualized for a typical warm-up curve in Figure 17.

The most dominant feature in Figure 16 is the smooth transition at about 75 K from a very homogeneous transmission distribution, given by normalization, to a rougher transmission distribution. This behavior can be explained very well by the collapse of superconductivity in the used high temperature superconducting microwave cables.

The vertical features at around 180 K are attributed to binning-algorithm errors and will not be discussed further.

Next, I would like to discuss features that need further investigation. For some frequencies, better transmission is obtained at higher temperatures, when the superconducting cables are in normal state. These features seem to be associated with a temperature dependence of the frequency. In particular, the frequency and temperature dependent features are magnified in the four insets of Figure 16. In itself, the FMR has no temperature dependent quantities, so these features must also be related to the transmission characteristics of the microwave cables.

An approach to explanation would be to assume an electro-magnetic resonator. In this case, the permittivity of the resonator would have to depend strongly on the temperature. Since the structure is in vacuum, only the cables and their terminations can form resonators, which depend on temperature and frequency.

At this point, further investigation is needed to determine the origin of these features. Also, a higher resolution measurement in the range from base temperature to about 10 K would be very interesting. In this temperature range, I expect a large number of interesting transmission features, especially in the order of magnitude of transmission variations due to FMR. Here I would like to emphasize the different orders of magnitude of transmissions variation caused by either temperature variations or typically measured FMR. Unfortunately, the measured warm-up was too fast for the slow frequency sweeps, which are optimized for a high dynamic range of transmission. Further, parameter optimization is needed for measurements in this low temperature range.

In early measurements on the HelioxVL setup I could see large differences in transmission compared to the FMR signal before and after helium transfer. During the transfer, the temperature in the dewar fluctuates quite a lot. Unfortunately, I did not log the temperature during these measurements and it remains questionable whether the presence of the transfer line might not also influence the applied magnetic field.

5 Results and Diskussion

In this Chapter, I will compare two datasets recorded for samples CPW2 and CPW3. Although many parameters differ in sample preparation and data collection (see Table 3 in the Appendix), these two samples are interesting for investigating the effect of two different Co thicknesses $d_{\text{CPW}2} = 32.5 \text{ nm}$ & $d_{\text{CPW}3} = 3 \text{ nm}$. Finally, I will use Kittel's equation 2.12 to quantify the saturation magnetization and anisotropy field.

First, I will focus on a qualitative description of the two datasets. Figure 18 shows the transmission of the two datasets, sample CPW2 (b) and CPW3 (c). Well connected minima can be observed in the FMR typical Y-shape. This shape already qualitatively fits the Kittel formula for an in-plane sample geometry of Co, see below. We can observe the already known noise induced by laboratory temperature variations in the form of typical vertical lines in both measurements. The CPW3 dataset was recorded over a much longer period of time, therefore the deep dark lines are much more frequent. Compared to the CPW2 dataset, we can also better observe a general day-dependent drift. As a reminder, the distance between two dark lines corresponds approximately to a recording time of 12 h. This behavior is consistent with Section 4.3.4.

The normalization transmissions T_{21}^0 are shown in Figure 18a. The first thing to notice here is the difference in signal size of about 20 dB. This is due to the fact that the CPW3 dataset was measured without the two -10 dB dampers (see Section 3.2). Next noticeable is the seemingly much smoother curve of the CPW2 sample. However, this was only measured at a frequency resolution of 250 MHz, while CPW3 was measured at a resolution of 20 MHz. This explains the apparent lower noise level.

Especially for the CPW2 measurement, a resonance around 18 GHz is particularly noticeable. The typical cavity length, corresponding to 18 GHz¹ is calculated as $\ell = c_0/2f = 1,65 \text{ cm}$. This corresponds to the distance between the plate to which the sample is mounted and the copper cup that shields the sample from thermal radiation. In the CPW3 sample, there is a similar feature at 16,86 GHz, which corresponds to a length of 1,76 cm. Note also the expression of the dips in the normalization transmission of the two measurements. For the CPW2 sample, the dip at 18 GHz is very pronounced, while for the CPW3 sample, the dip at 16.86 GHz is almost lost in the noise. It is conceivable that the cup was not screwed on quite correctly and is slightly tilted. As a result, the finesse of the cavity of sample CPW3 is not as good as that of sample CPW2 and thus there is much less transmission loss.

With the resonance just discussed, another conspicuous feature can be observed on the maps further out at 642 mT (CPW2) and at 597 mT (CPW3), respectively. This is most likely a volume-specific ferromagnetic resonance effect. For clarity, I have plotted the theoretical Kittel formula, for a spherical sample geometry, given by

$$\omega_{\text{res}}^{\circ} = \gamma\mu_0 H \quad (5.1)$$

in magenta. The signal strength is much more pronounced in CPW2, with $d_{\text{CPW}2} = 32.5 \text{ nm}$ Co, which is in good agreement with a volume-dependent effect. Nevertheless, we should keep in mind that it could also be a Zeeman splitting of some state, since it has the same shape.

Next, I want to quantify the saturation magnetization and the uniaxial anisotropy field. For this I use the positions of the minima obtained in Section 4.1 and marked in Figure 9. I plot the minima and fit them with the Kittel formula for an in-plane sample geometry in Figure 19. This formula is

¹Other measurements with higher frequency resolution on the same sample tend to detect this feature at 18, 10(2) GHz.

given by

$$\omega_{\text{res}}^{\parallel} = \gamma \mu_0 \sqrt{(H + H_{\text{ani}})(H + H_{\text{ani}} + M_s)} . \quad (5.2)$$

The obtained saturation magnetizations are $M_s = 15.9(4)$ kOe / $\mu_0 M_s = 1.59(4)$ mT for CPW2 and $9.4(6)$ kOe for CPW3². This is in contrast to measured magnetization of Co on GaAs substrate by Tinouche et al. They measured an increase in magnetization to smaller Co film thicknesses, $20\text{ nm Co} \triangleq 16.7$ kOe and $35\text{ nm Co} \triangleq 7.5$ kOe. Jamali et al. report a saturation magnetization of 13.8 kOe for a 1 nm thick Co film sputtered on graphene. Asu et al. report a saturation magnetization of 17.3 kOe for nano-crystalline bulk Co. All of these values are on the same order of magnitude as the measured saturation magnetizations. [61, 62, 63]

The uniaxial anisotropy field H_{ani} for the CPW2 sample is $-1.4(38)$ mT for the CPW3 sample $H_{\text{ani}} = 32(12)$ mT. This can be explained in terms of the form anisotropy, which increases for smaller thickness confinement of the sample geometry. Thus, it is expected to find a larger fraction of the volumetric resonance in sample CPW2, but as well as a lower anisotropy. In contrast, in the Co layer in sample CPW3, which is thinner by a factor of 11, the volume-specific fraction of the resonance is hardly measurable and a much higher anisotropy is observed respectively. Alameda et al. have found uniaxial anisotropy fields of 1.5 , 3 and 15 mT for Co thicknesses of 100 , 45 and 15 nm. Both the order of magnitude and the general trend are confirmed by my measurements. [64]

²The magnetization M is usually written in $1\text{ A/m} = 4\pi \cdot 10^{-3}\text{ Oe}$, the magnetic field $\mu_0 H$ in Tesla $1\text{ T} = 10^4\text{ Gs}$. However, the magnetic field can be written as $\mu_0 H(\text{Gs}) = \mu_0 \cdot H(\text{Oe})$.

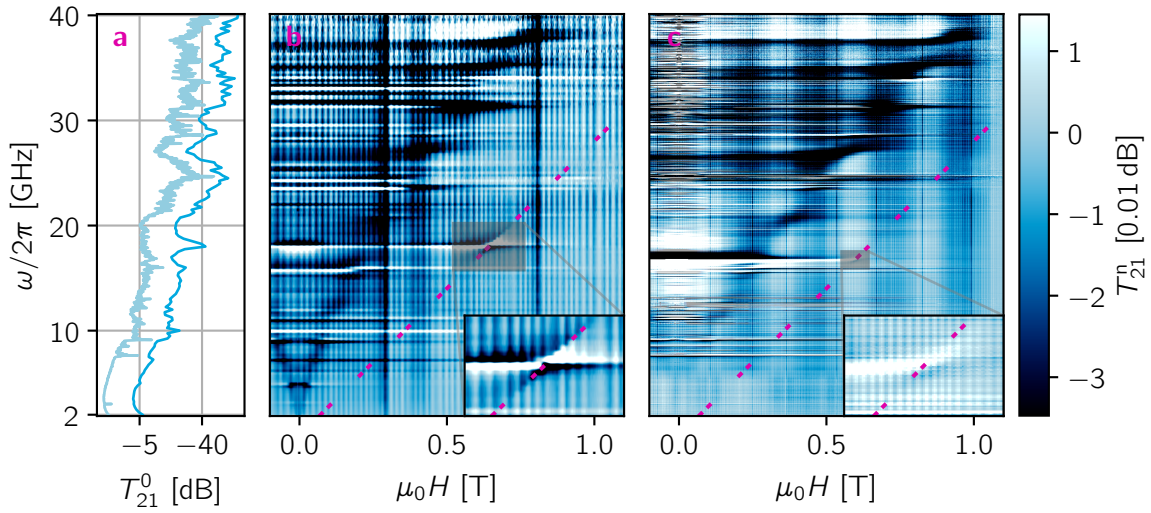


Figure 18 Normalized transmission as a function of frequency $\omega/2\pi$ and magnetic field $\mu_0 H$. In panel **a** the normalization transmission T_{21}^0 , in **blue** for CPW2 and in **light blue** for CPW3, for a magnetic field of $H_n = 1.1$ T are shown. The two measured transmission maps T_{21}^n for samples CPW2 with 32.5 nm Co and CPW3 with 3 nm Co are shown in panel **b** & **c**. Additionally, in **magenta** the theory curve for ω_{res} (eq. 5.1) is shown. The respective insets zoom in on the features in which the correlation of the data and the theory is well evident.

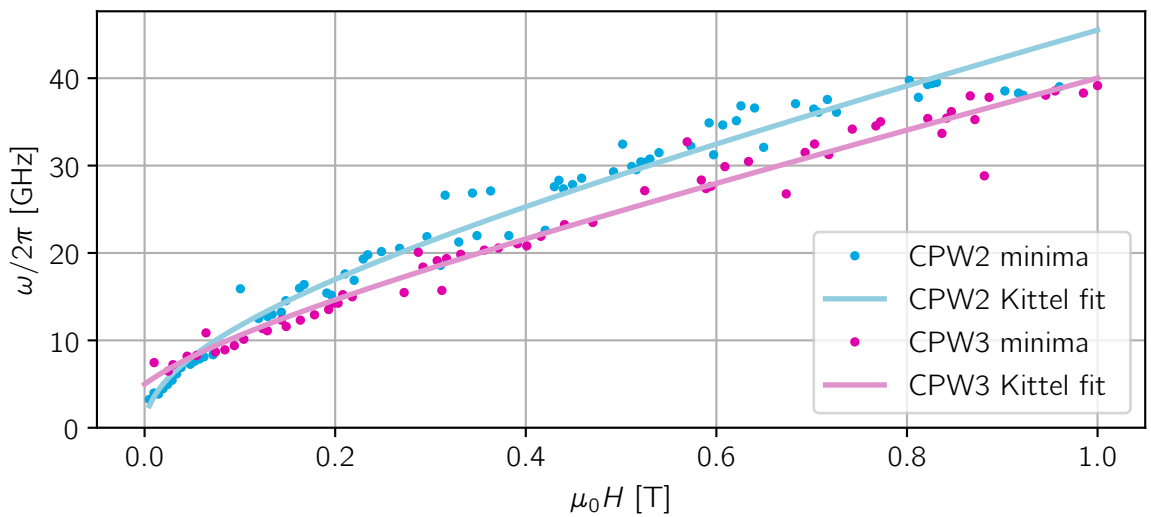


Figure 19 Transmission minima obtained as a function of frequency and magnetic field for samples CPW2 (**blue**) and CPW3 (**magenta**). The minima were fitted with the Kittel formula $\omega_{\text{res}}^{\parallel}$, according to equation 5.2 (**light blue** and **light magenta**). For sample CPW2, the uniaxial anisotropy field is $\mu_0 H_{\text{ani}} = -1.4(38)$ mT and the magnetization is $M_s = 15.9(4)$ kOe. For sample CPW3, $\mu_0 H_{\text{ani}} = 32(12)$ mT and $M_s = 9.4(6)$ kOe are found.

6 Conclusion

The goal of my work was to investigate the ferromagnetic resonance (FMR) of a superconductor/ferromagnet/superconductor (S/F/S) contact. This was achieved for reasonable film thicknesses down to 3 nm of Co. This thickness is comparable to the coherence length of singlet Cooper pairs in Co. Furthermore, I was able to obtain both the saturation magnetization and the single-axis anisotropy field of a 30 and 3 nm thin Co layer. Likewise, I was able to obtain and explain volume-dependent components of the FMR.

However, only very-large-area sample geometries were investigated. For samples that are also designed for electronic transport measurements, this area must be reduced by several orders of magnitude. This leads to two challenges: First, the FMR signal strength scales with area, since the absorption in the ferromagnet is proportional to the sample volume and therefore to the signal strength. This makes it much more difficult, if not impossible, to resolve the FMR with the vector network analyzer (VNA). Second, the smaller sample geometry may change the magnetization, the uniaxial anisotropy field, and thus the FMR frequency, with no further prediction possible. Hence, for smaller sample geometries the FMR has to be redetermined, to exclude the effect of further geometrical constraints. To increase the volume and signal-to-noise ratio of a very small sample without changing its geometry, the possibility would be to use a whole series of the samples under the CPW.

In the future, only the area under the inner conductor, near the center, should be used. In this case, the alternating magnetic field would become more homogeneous and the signal-to-noise ratio of the FMR could increase.

Furthermore, many valuable insights into the setups and devices used could also be gained. I was able to show qualitatively that the HelioxVL setup has magnetic components. FMR signals of the same sample could be reproduced in both setups. I was also able to compare the frequency and magnetic field sweep modes. Likewise, I was able to narrow down useful measurement parameters and make a clear recommendation for future measurements. In addition, I investigated the coupling between laboratory temperature and noise of the measurement electronics used. I was able to successfully apply the method of frequency domain reflectometry. This proved to be a useful tool to locate interruptions in the measurement line due to thermal shrinking upon cooling. I was also able to show a temperature dependence of the transmission through the measurement line and the sample. It is of great interest to repeat the measurements in a lower temperature range and study in more detail.

In summary, my findings on ferromagnetic resonance will find their way into ongoing research on dynamic ferromagnetic Josephson junctions.

Appendix

In Figure 20 you can find the differences in line-by-line averaging for pre-normalized transmission by fixed-field reference method or moving-field reference method.

Figure 21 shows two transmission measurements, in panel b without and in panel c with pre-amplifier. Beside that, they are made with exactly the same sample CPW3, the same setup BlueFors and the same parameters, see column CPW3 in Table 3, separated by a warm-up and cool-down process. For frequencies above 30 GHz, the measurement with pre-amplifier clearly shows a more recognizable FMR signal. However, in panel b, the most recent¹ measurement raises more questions. Features that need further investigation are on the one hand the sudden change in transmission at around 0.5 T, on the other hand, the feature at around 21 GHz. Otherwise, similar features around 21 GHz were identified as cavity modes, but shifted by a few GHz. At this point, further research should be done to see if they can be attributed to cavity modes or other effects.

Details and parameter of the sample preparation of CPW2, can be found in Table 2. In Table 3 you can find the differences in sample preparation and data acquisition for the samples CPW3 and CPW2, compared in Chapter 5.

Furthermore, I want to present some self-written device drivers and packages. First will be the magnet driver IPS120_10, then the ZNB40 VNA driver for frequency sweeps, followed by the GIR2002 thermometer driver. In the end, you can find my corporate design color package, which maps the given colors in such a way, that homogeneous gradients are achieved. All colors in each data plot in this Thesis are done with this package.

¹The measurement was completed just one week before submission.

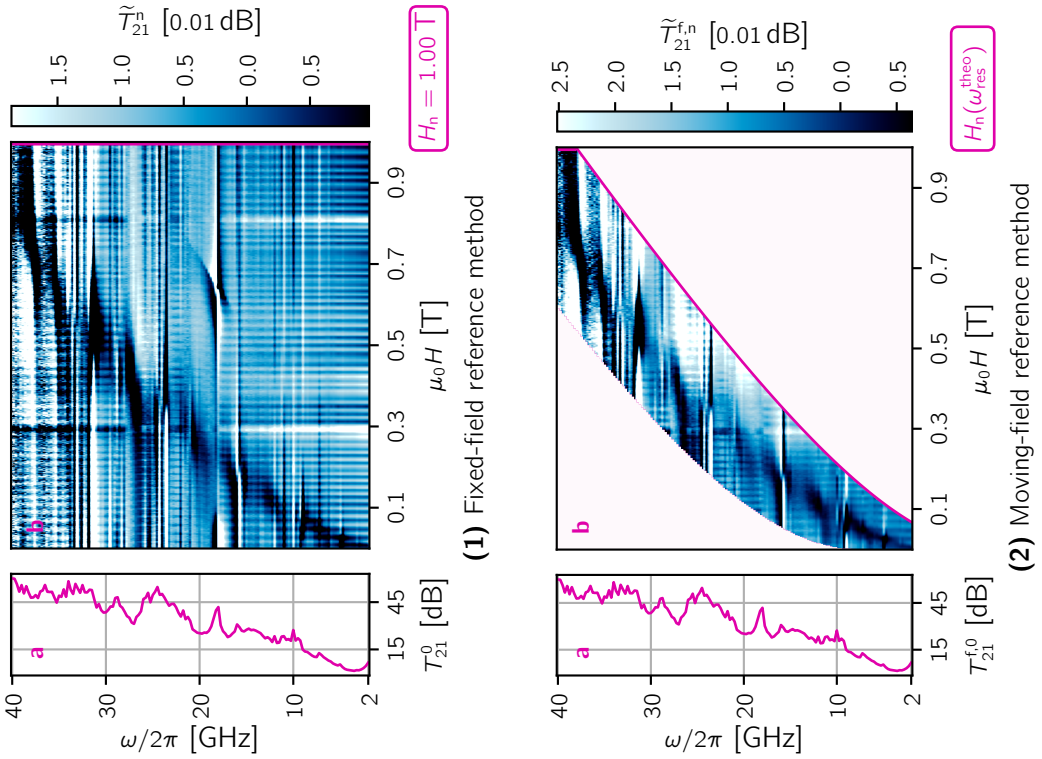


Figure 20 Line-wise frequency and magnetic field averaged transmission of sample CPW2, normalized as in Figures 10.1 and 10.1. In **(1)** and **(2)** the two normalization methods fixed-field reference and moving-field reference are shown. The normalization transmission T_{21}^0 is shown in **a** and the averaged and normalized transmission \tilde{T}_{21}^n is shown in **b**. In addition, the course of the magnetic field H_n selected for normalization is shown in **magenta**.

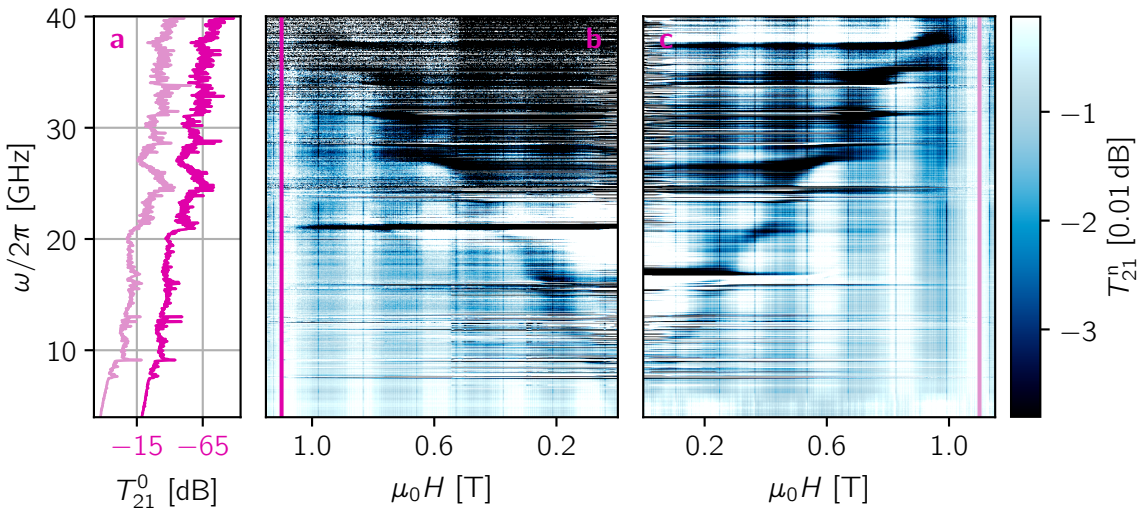


Figure 21 Normalized transmission T_{21}^n measured without **(b)** and with pre-amplifier **(c)** as a function of frequency $\omega/2\pi$ and magnetic field $\mu_0 H$ for the sample CPW3, setup BlueFors and with the same parameters. The measurements are separated by a warm-up and cool-down process. The normalization transmissions T_{21}^0 for a fixed magnetic field of $H_n = 1.15$ T are shown in **a**.

Table 2 Preparation steps of sample CPW2

substrate	Si wafer with 200 nm SiO ₂
photoresist	'AR-P 5350 Photoresist' [65] spin coated: 60 s at 5000 rpm baked: 4 min at 95 °C
mask design	'Inkscape' [66] file: *.png & 0.71 µm pixels structure: white on black
exposure	'Smart print' [67] import: 'stitch black' & 'High res.' pixel red. & field con. cor.: 10 objective & time: ×10 & 0.9 s
development	'AR 300-26' [68] dilution: 1 + 6 parts distilled water development time: by sight, ≈ 40 s
evaporation	100 nm Al (thermal) 32.5 nm Co (electron-beam) 100 nm Al (thermal)
lift-off	acetone bath: ≈ 5 min at 60 °C
PI layer	spin coated: 90 s at 5000 rpm pre-baked: 5 min at 130 °C vacuum-bake-out [69]
CPW	3 nm titanium (electron-beam) 50 nm gold (electron-beam)

Table 3 Differences in sample preparation and data acquisition for the samples CPW2 and CPW3. Transmission data are shown in Figure 9 & 18. (VNA sweep time means the time needed to obtain all data for a fixed magnetic field.)

	CPW2	CPW3
Co thickness covered in Pi layer	32 nm 2 · 100 nm Al yes	3 nm 120 nm Cu no
dampers in setup pre-amplifier T_{FMR}	yes yes 4 K	no yes (tempered at 25 °C) ≈ 95 mK
H range ΔH	−1.3 to 1.3 T 0.5 mT	−0.1 to 1.2 T 0.5 mT
f range Δf	2 to 40 GHz 250 MHz	2 to 40 GHz 20 MHz
VNA power VNA bandwidth VNA averaging VNA sweep time	−5 dBm 500 Hz 160 53.1 s	−5 dBm 30 Hz 3 208.5 s
H_{ani} M_s	−1.4(38) mT 15.9(4) kOe	32(12) mT 9.4(6) kOe

```

1 # -*- coding: utf-8 -*-
2 """
3 Current Version from: 04.02.'21
4 - Fixes possible 'quenching, when connection is lost' BUG
5 - Check for Helium Level Shut Down and Switch Heater
6
7 Current Version from: 25.09.'20
8 Features:
9 - implementing factor for max rate
10
11 Current Version from: 06.08.'20
12 Features:
13 - printer implemented
14
15 Version from: 06.07.'20
16 Features:
17 - negative magnetic field support
18 - reducing to function goto with optional rate input
19 - change rate on the fly, while in max mode
20 - "printer" consistency
21 - error if field is to high
22
23 @author: Oliver I.
24 Many Thanks to: Lukas Kammermeier
25 """
26
27 import pyvisa, sys
28 import numpy as np
29 from time import sleep
30
31 #####IPS120_10#####
32 class IPS120_10():
33     """
34     # e.g.: Set magnetic field
35     from driver.IPS120_10 import IPS120_10
36     magnet=IPS120_10()
37     magnet.reinitialize()
38     magnet.goto(0.1,factor=.7)
39     magnet.readfield(printer=True)
40     magnet.turn_off()
41     magnet.exit()
42     """
43     def __init__(self, GPIB_No=25):
44         rm=pyvisa.ResourceManager()
45         inst=rm.open_resource('GPIBO::%i::INSTR'%GPIB_No,
46                               read_termination='\r',
47                               write_termination='\r')
48         inst.timeout=2000
49         self.inst=inst
50
51     def initialize(self, printer=False):
52         """
53             Initializes Magnet.
54         """
55         # Check for Helium Shut Down
56         helium_alarm=int(self.inst.query('X')[6])
57         if helium_alarm>3:
58             sys.exit('Helium Shutdown: Not enough Helium!')
59
60         # Initializes
61         try:
62             self.inst.write('$C3')      #remote & unlocked
63             sleep(0.1)
64             self.inst.write('$Q4')      #four digits extended resolution

```

```

65             self.inst.write('$M1')      #set mode, units "tesla", fast
66             sleep(0.1)
67             self.inst.write('$H1')      #switch heater on
68             sleep(0.1)
69             self.inst.write('$A0')      #hold operation
70             self.inst.heater=True      # switch heater on
71             if printer==True:
72                 print('Magnet Initializing.. Please Wait 10s')
73             for i in range (10): #wait for 10s
74                 sleep(1)
75                 pass
76             except:
77                 print('ERROR: magnet initialization failed')
78                 return False
79
80             # Check for Switch Heater
81             switch_heater=int(self.inst.query('X')[8])
82             if switch_heater!=1:
83                 sys.exit('Error: Switch Heater is not on!')
84
85             if printer==True:
86                 print('Done Initializing')
87
88         def turn_off(self, printer=False):
89             """
90                 Closes Connection and makes magnet ready to shut down.
91             """
92             self.goto(0)
93             sleep(0.1)
94             self.inst.write('$A0')      #hold operation
95             sleep(0.1)
96             self.inst.write('$H0')      #Heater off
97             sleep(0.1)
98             self.inst.write('$C2')      #remote & unlocked
99             self.inst.close()          #close connection with magnet
100            if printer==True:
101                print('Connection to magnet closed, Turn off power!')
102
103        # Simple function to read/set the current rate/field
104        # all numbers dimension is T/min
105        # printer=False prevent from printing (default: True)
106        # redundant check if setrate is higher than 0.723 (ScheerIII)
107        # TODO make them consistent!
108
109        def readrate(self, printer=False):
110            rate=float(self.inst.query('R9')[1:])
111            if printer==True:
112                print('current rate is %5.4f T/min.'%rate)
113            return rate
114
115        def setrate(self, sweprate, printer=False):
116            self.inst.write('$T%4.3f'%sweprate)
117            sleep(0.1)
118            rate=self.readrate(printer)
119            return rate
120
121        def readfield(self,printer=False):
122            field=float(self.inst.query('R7')[1:])
123            if printer==True:
124                print('current field is %5.4f T'%field)
125            return field
126
127        def setfield(self, target, printer=False):
128

```

```

129     self.inst.write('$J%f'%target)
130     new_target=float(self.inst.query('R8')[1:])
131     if printer==True:
132         print('target field is %.4f T '%new_target)
133     #activate "GOTO SET"
134     self.inst.write('$A1')
135     return new_target
136
137 def goto(self,target,rate='max', factor=.9, printer=False):
138     """
139     Ramps with either a given rate, or maximum rate,
140     optional reduced by factor(0<facotr<=1, default:.9).
141     """
142     if rate=='max':
143         self.goto_max(target, factor, printer)
144     else:
145         self.goto_set(target, rate, printer)
146
147 def goto_set(self, target, rate, printer=True):
148     """
149     Ramps to field, with given rate.
150     Approximates remaining time.
151     """
152     self.setrate(rate,printer)
153     self.setfield(target,printer)
154     check=False
155     while check==False:
156         field=self.readfield(printer)
157         time=60*(abs(target-field)/rate)
158         if np.abs(field-target)< 3e-4:
159             if printer==True:
160                 print('\nTarget Field reached...OK')
161             check=True
162             break
163         else:
164             if printer==True:
165                 print('Field is %.6.4f T, remaining time is %.1f s'%(field,time),end='\r')
166             sleep(0.1)
167             pass
168     return field
169
170 def find_pos(self, field, spez_field):
171     """
172     Help function, to find field segment.
173     """
174     pos=np.nan
175     len_spez_field=len(spez_field[1:-1])
176     if field is not np.nan:
177         for i in range(len_spez_field-1):
178             if field<=0: check=(field>=spez_field[i+1])&(field<spez_field[i+2])
179             else: check=(field>spez_field[i+1])&(field<=spez_field[i+2])
180             if check: pos=i
181         else: print('Error: No field given to find pos')
182     if pos==np.nan: print('Error: Invalid segment!')
183     return pos
184
185 def goto_max(self, target, factor=.9, printer=True):
186     """
187     Ramp field with maximum rampage,
188     reduced by factor (0<factor<=1, def:.9).
189     Don't quench, when Connection is lost.
190     """
191
192     # Scheer III Specification
193     spez_field=np.array([-np.inf,-12,-9.6,-7.8,-7.8,9.6,12,np.inf])
194     spez_rate=np.array([.1205,.2410,.723,.2410,.1205])
195     #
196     # Testing spezification
197     spez_field=np.array([-np.inf,-.12,-.1,-.08,.08,.1,.012, np.inf])
198     spez_rate=np.array([.3,.5,.7,.5,.3])
199
200     # testing reasonability of factor
201     if (factor<=0)|(factor>1):
202         factor=.9
203         print('Not good: factor = .9 !')
204     if factor>.9:
205         print('Sure?')
206
207     # check for position and reasonability target
208     pos_target=self.find_pos(target,spez_field)
209     if pos_target is not np.nan:
210
211         # check for field
212         field=self.readfield(printer=False)
213
214         # check if field is reached yet
215         check=False
216         while check==False:
217
218             # empties annoying buffer
219             try:
220                 self.inst.timeout=100
221                 blubb=self.inst.read_raw()
222             except:
223                 blubb=3
224             self.inst.timeout=2000
225             sleep(.1)
226
227             # check for field
228             field=self.readfield(printer=False)
229
230             # check for segment position
231             pos_field=self.find_pos(field,spez_field)
232
233             # check for segment position in range
234             if pos_field==np.nan:
235                 print('Aborted: Current magnetic field out of range!')
236
237             # set rate
238             rate=spez_rate[pos_field]*factor
239             self.setrate(rate, printer=False)
240
241             # check for segment border, set field
242             if pos_field==pos_target:
243                 self.setfield(target, printer=False)
244             else:
245                 if field<target:
246                     inter=spez_field[pos_field+2]+1e-4
247                 elif field>target:
248                     inter=spez_field[pos_field+1]-1e-4
249                 else:
250                     print('Error: No intermediate Field!')
251                     inter=field
252             self.setfield(inter, printer=False)
253
254             # do cosmetics
255             if printer==True:
256                 print('Field: %+07.4f/%+07.4f T'%(field,target),end='\r')

```

```

256         # is it reached yet?
257         if np.abs(field-target)< 1e-4:
258             check=True
259             if printer==True:
260                 print('\nField is reached!')
261
262     # check for position and reasonability target
263     else:
264         print('Error: Please set reasonable magnetic Field!')
265
1 # -*- coding: utf-8 -*-
2 """
3 Created on Fri Jun 26 15:06:25 2020
4
5 Bugfix 09.12.2020
6     # fsweep
7     - sweep time -> timeout
8     catch exception for high bandwidth and averaging
9
10 current Version 2.0 from 21.11.2020
11 Features:
12     - use PyVISA protocoll instead of Rohde/Schwarz protocoll
13     # frequency sweep mode
14     - reducing s-parameter sweep to S21 (due preamplifier)
15     - saving complex and real part seperately
16     - saving temperature as well
17     - reducing config file to essential
18     - saving bfield with max number of digits
19     - printer option
20     - autoscaling at vna
21
22 @author: Oliver I.
23 Many Thanks to: Lukas Kammermeier und Lukas Siedentop
24
25 e.g.:
26 # Measure f_sweep
27 from ZNB40 import ZNB40
28 vna=ZNB40(IP='192.168.1.104')
29 vna.enter()
30 config=vna.setup_fsweep(start=2e6,
31                         stop=4e10,
32                         points=1e3,
33                         bandwidth=1e3,
34                         power=-10,
35                         average=0,
36                         printer=False,
37                         saveconfig=True)
38 vna.measure_fsweep(sample_name='test',
39                     H=-99.9999,
40                     T=0,
41                     plotter=True,
42                     savefile=False,
43                     printer=False)
44 vna.exit()
45 """
46 #####
47 ##### import os
48 import pandas as pd
49 import numpy as np
50 import matplotlib.pyplot as plt
51 import json
52 from datetime import datetime
53
54 import pyvisa
55 style='test'
56 plt.style.use('driver\%s.mplstyle'%style)
57
58 class ZNB40():
59
60     ##### general stuff
61     def __init__(self, IP='192.168.1.104'):
62         # black VISA magic
63         # watch out for VISA and stuff
64         # else dead
65         rm=pyvisa.ResourceManager()
66         inst=rm.open_resource('TCPIPO::'+IP+'::inst0::INSTR')
67         #inst=rm.open_resource('TCPIPO::'+IP+'::hislip0')
68         self.inst=inst
69         self.inst.timeout=1e5
70
71     def enter(self):
72         # reset the device
73         self.inst.write('*RST')
74         # delete all old traces
75         self.inst.write('CALC:PAR:DEL:ALL')
76         # turn continuous measurement off
77         self.inst.write('INITiate1:CONTinuous OFF')
78         # turn Display to remote control
79         self.inst.write('SYSTem:TSLock SCReen')
80         # close soft tool menu
81         self.inst.write('SYSTem:DISPlay:BAR:STOols OFF')
82         # displaying the data increases measurement time
83         self.inst.write('SYSTem:DISPlay:UPDate OFF')
84
85     def exit(self):
86         # unlock and turn on screen for local operation
87         self.inst.write('SYSTem:TSLock OFF')
88         self.inst.write('SYSTem:DISPlay:UPDate ON')
89         self.inst.write('SYSTem:DISPlay:BAR:STOols ON')
90
91     ###### frequency sweep mode
92
93     def setup_fsweep(self,
94                      sample_name='no_sample_name_provided',
95                      start=2e6,
96                      stop=4e10,
97                      points=1e3,
98                      bandwidth=1e3,
99                      power=-10,
100                     average=0,
101                     printer=False,
102                     saveconfig=True):
103
104         # setup S21 scattering parameter
105         self.inst.write("DISP:WIND:STAT ON")
106         self.inst.write("CALC1:PAR:SDEF 'Tr1', 'S21'")
107         self.inst.write("DISPlay:WINDOW:TRAC1:FEED 'Tr1'")
108
109         # setup configuration
110         self.inst.write("SENSe1:FREQuency:STARt %i Hz"%start)
111         self.inst.write("SENSe1:FREQuency:STOP %i Hz"%stop)
112         self.inst.write("SENSe1:SWEep:POINTs %i"%points)
113         self.inst.write("SENSe1:BANDwidth %i Hz"%bandwidth)
114
115
116
117

```

```

118     self.inst.write("SOURce1:POWer %i dBm"%power)
119     time=self.inst.query('SENSe1:SWEep:TIME?')
120
121     # caring about averaging
122     if average >1:
123         self.inst.write("SENSe1:AVERage:COUNT %i"%average)
124         self.inst.write("SENSe1:AVERage:STATE ON")
125         self.inst.write("SENSe1:AVERage:CLEar")
126         self.inst.write("SENSe1:SWEep:COUNT %i"%average)
127     else:
128         self.inst.write("SENSe1:AVERage:STATE OFF")
129
130     # sets timeout time between measurments to zero
131     self.inst.write("SENSe1:SWEep:TIME:AUTO ON")
132     #self.inst.write('SYSTem:DISPlay:BAR:STOols OFF')
133     #self.inst.write('SYSTem:DISPlay:UPDate ONCE')
134
135     # gets maximum timeout time, to prevent errors during long time meas.
136     time=float(self.inst.query('SENSe1:SWEep:TIME?'))
137     if average >1:
138         self.inst.timeout=int((time*average*2.5+10)*1000)
139     else:
140         self.inst.timeout=int((time*2.5+10)*1000)
141
142     # print configuration parameter
143     if printer==True:
144         print('\nThe parameter are:')
145         print('start frequency = %i Hz'%start)
146         print('stop frequency = %i Hz'%stop)
147         print('sweep points = %i'%points)
148         print('bandwidth = %i Hz'%bandwidth)
149         print('power = %i dBm'%power)
150         print('\nThe cycle will need %.1f s.'%time)
151
152     # builds config file
153     date=str(datetime.now())
154     config={'ZNB40':{'frequency sweep':
155         'sample_name':sample_name,
156         'timestamp_setup':date,
157         's_param':'S21',
158         'start':int(start),
159         'stop':int(stop),
160         'points':int(points),
161         'bandwidth':int(bandwidth),
162         'power':power,
163         'average':average,
164         'sweptime':time}}
165
166     # Save Config File
167     if saveconfig==True:
168         # append config file to current conig.json
169         with open('vna_fsweep_config.json','a+') as f:
170             json.dump(config,f,indent=1)
171
172         if printer==True:
173             print('\nSaved configuration successfully!')
174     return config
175
176 def measure_fsweep(self,
177     config={'sample_name':'no_config_delivered'},
178     H=-99.9999,
179     T=0,
180     plotter=False,
181     savefile=True,
182
183         printer=False
184     ):
185
186         # initialize measurement
187         self.inst.write("INITiate")
188         self.inst.write('*WAI')
189
190         # gets x-axis/frequency data
191         # freq = self.inst.query('CALC1:DATA:STIM?')
192         # freq=np.fromstring(freq, dtype='float64', sep=',')
193         freq=np.linspace(config['start'],config['stop'],config['points'])
194
195         # gets S21 parameter and save them as real and imag
196         query_str = "CALC1:DATA:TRACe? 'Tr1', SDAT"
197         sdata = self.inst.query(query_str)
198         data = np.fromstring(sdata, dtype='float64',sep=',')
199         real, imag = data[:,0], data[:,1]
200
201         # builds dataframe with x-axis/frequency
202         datafram=pd.DataFrame(data={'freq':freq,
203                                     'Re_S21':real,
204                                     'Im_S21':imag},
205                                     dtype='float64')
206
207         self.inst.write('SYSTem:DISPlay:UPDate ONCE')
208         self.inst.write('SYSTem:DISPlay:BAR:STOols OFF')
209         self.inst.write('DISP:TRAC1:Y:AUTO ONCE')
210         # plots plot to lookylook
211         if plotter==True:
212             plt.figure(1)
213             plt.plot(freq,10*np.log(np.abs(real+imag*j)),'.',
214                         label=str(datetime.now()))
215             plt.grid()
216             plt.title('Insertion loss of forward transmission')
217             plt.ylabel('$I_{S_{21}}|\$ [dB]$')
218             plt.xlabel('$f$ [Hz]')
219             plt.legend(loc=1)
220
221         if savefile==True:
222             if not os.path.exists('fsweep_data'):
223                 os.makedirs('fsweep_data')
224             Hstring='H%07i'%int(float(H)*10000)
225             name='fsweep_data/%s_%s_T%05i_%s.csv'%(config['sample_name'],
226             Hstring,int(float(T)*1000),str(str(datetime.now()).replace(':','-'))[-7])
227
228             # save data
229             pd.DataFrame.to_csv(dataframe,name)
230             del dataframe
231             if printer==True:
232                 print('\nSaved Data successfully!')
233
1 import serial
2 import numpy as np
3 import os
4 from time import sleep
5 from datetime import datetime
6 """
7 author: Oliver Irtenkauf
8 date: 21.01.2021
9
10 TODO:
11 - datetime format einheitlich. check for easy read function.
12 - check for filt: off

```

```

13 - check for seri setting
14
15 Usage of GIR2002, with EBW3 adapter, thermo couple Type K
16 TC an Pin 10 und 11, Kabel: grün/weiß -> TypK, more @ evaporater cabinett
17 setup rear side + button2:
18 InP: t.tc
19 SEns: NiCr-Ni (type K) [-70...-1250°C, -200...12850°C]
20 rES: 0.1
21 Unit: °C
22 FiLt: 0.01
23
24 (Explanation: this digital filter is a digital replica of a low pass filter.
25 Note: If the digital filter is off the internal mains hum suppression of the GIR2002 is
deactivated. This adjustment is ideal for fastest response to even small changes of
the signal, but the display and the analog output gets more turbulent. Therefore the
filter should set to at least 0.01 for ordinary application A filter value of at
least 0.1 is recommended for the input type S.)
26
27 rear side + button1:
28 outP: no
29
30 manuals:
31 GIR2002_e.pdf
32 GMH3xxx_interface_without_DLL.pdf
33 """
34 #####
35 #####
36 class GIR2002(serial.Serial):
37     """
38     # Example:
39     from drivers.GIR2002 import GIR2002
40     thermo=GIR2002(com_port=11)
41     thermo.logging(path='thermo_data',
42                     name='_pos_is_free_hanging',
43                     avg=100,
44                     sleeper=0,
45                     show_progress=True)
46     # thermo.close()
47     """
48     def __init__(self, com_port=11):
49         """
50             initialize black serial magics
51         """
52         serial.Serial.__init__(self, 'COM%i'%com_port)
53         self.baudrate = 4800
54         self.bytesize = serial.EIGHTBITS
55         self.parity = serial.PARITY_NONE
56         self.stopbits = serial.STOPBITS_ONE
57         self.timeout = 1
58         self.xonxoff = False
59         self.rts = False
60         self.dtr = True
61         self.inter_byte_timeout = None
62         self.reset_input_buffer()
63         self.reset_output_buffer()
64         self.breaker=False
65
66     def exit(self):
67         self.close()
68
69     def value(self):
70         """
71             get Thermodata.
72

```

```

73     try 'GMH3xxx - Serial Interface'
74     aka GMH3xxx_interface_without_DLL.pdf
75     bugs with decimal point: just ignore,
76     because. \pm 0.1°C is as good as it gets, with Type K
77     """
78     self.write(bytarray((254,0,61))) #255 - address 1, command 0, crc 61
79     response=bytes(self.read(6))
80     integer=(256*(255-response[3])+response[4])&16383-2048
81     value=integer/10
82     # spez={'49152':1000, '32768':100, '16384':10, '0':1}
83     # decimal_point='%i'%'((256*255-response[3])&49152)
84     # value=integer/spez[decimal_point]
85     # print(value, end='\r')
86     except:
87         value=np.nan
88     return value
89
90     def show_value(self):
91         """
92             simple live monitoring
93         """
94         i=0
95         while True:
96             i=(i+1)%4
97             progress='\\/-|'
98             T=self.value()
99             if self.breaker==True:
100                 break
101             if T is not np.nan:
102                 print('%s T = %2.1f °C  %(progress[i],T), end='\r')
103             else:
104                 print('%s lost signal  %progress[i], end='\r')
105
106     def average_value(self, avg=10, sleeper=.01):
107         """
108             simple average method to decrease data pillage
109         """
110         if avg>1:
111             T=0
112             for i in range(avg):
113                 sleep(sleeper)
114                 T=T+self.value()
115             T=T/avg
116         elif avg==1 or avg==0:
117             sleep(sleeper)
118             T=self.value()
119         else:
120             print('try reasonable number!')
121             T=np.Nan
122         return T
123
124     def logging(self,
125                 path='thermo_data',
126                 name='',
127                 avg=100,
128                 sleeper=0,
129                 show_progress=True):
130         """
131             simple temperature logging.
132             file structure, like BlueFors T logging
133             day,time,T [°C]
134         """
135         if not os.path.exists(path):
136

```

```

137     os.makedirs(path)
138     name='GIR2002_log%_s.csv' %(name,
139         str(datetime.now()).replace(':', '_')[-7:])
140     i=0
141     progress='\\-|'
142     while True:
143         if self.breaker==True:
144             break
145         try:
146             T=self.average_value(avg=avg, sleeper=sleeper)
147             if show_progress is True:
148                 i=(i+1)%4
149                 if T is not np.nan:
150                     print('%s T = %2.3f °C  %(progress[i],T), end='\r')
151                 else:
152                     print('%s lost signal  %(progress[i], end='\r')
153             if T is not np.nan:
154                 now=datetime.now()
155                 now=now.strftime('%d-%m-%y,%H:%M:%S')
156                 with open('%.s/%s'%(path,name), 'a') as fd:
157                     fd.write('%.s,%f\n'%(now,T))
158         except:
159             print('no signal')

1  '''version from 11.03.21
2 author: Oliver Irtenkauf
3
4 features: Coporate Design Colors of University Konstanz
5
6 for images with a gradient from black to blue to white use cpd.images(color='seeblau')
7 you can choose from the colors: color='seeblau' (default) or 'magenta' and 'grey'
8 you can invert those color bars by setting cpd.images(inverse=True)
9
10 for curves with a color gradient from blue to grey use cpd.curves()
11 you can choose from the colors: color='seeblau' (default) or 'magenta' and 'black'
12 in case you want the exact seeblau100, seeblau65 and seeblau35 colors use
13 cpd.curves(color='seeblau')(1-xx/100)
14
15 known bugs:
16 cpd.curves()(1)=cpd.curves()(0)
17
18 ...
19 import matplotlib.pyplot as plt
20 import numpy as np
21 from matplotlib import gridspec, cm
22 from matplotlib.colors import ListedColormap
23 try:
24     plt.style.use('thesis_half.mplstyle')
25 except:
26     print('no style found')
27
28 def curves(color='seeblau'):
29     # corporate design (for curves)
30     if color=='seeblau':
31         H,V,S=.5409,.8784,np.linspace(1,0,256)
32         R,G=V*(1-S),V*(1-S*(H*6-np.floor(H*6)))
33         B,A=V*np.ones(256),np.ones(256)
34     elif color=='magenta':
35         H,V,S=.5409,.8784,np.linspace(1,0,256)

36         G,B=V*(1-S),V*(1-S*(H*6-np.floor(H*6)))
37         R,A=V*np.ones(256),np.ones(256)
38     elif color=='black':
39         R=np.linspace(0,.65,256)
40         G,B=R,R
41         A=np.ones(256)
42         S=np.linspace(1,0,256)
43     else:
44         print("Please choose color from: 'seeblau', 'magenta' or 'black'")
45     cpd_curves = ListedColormap(np.array([R,G,B,A]).T)
46     return cpd_curves
47
48 def images(color='seeblau', inverse=False):
49     # corporate design (for images)
50     if color=='seeblau':
51         R=np.array([-89,0,89,160,200,255])/256
52         G=np.array([0,154,182,211,229,292])/256
53         B=np.array([0,209,220,230,239,305])/256
54         x=np.array([0,2.4,2.9,3.7,4.2,5])/5
55         polyRcoeff=np.polyfit(x,R,deg=4)
56         polyGcoeff=np.polyfit(x,G,deg=4)
57         polyBcoeff=np.polyfit(x,B,deg=4)
58     elif color=='magenta':
59         R=np.array([0,209,220,230,239,305])/256
60         G=np.array([-89,0,89,160,200,255])/256
61         B=np.array([0,154,182,211,229,292])/256
62         x=np.array([0,2.4,2.9,3.7,4.2,5])/5
63         polyRcoeff=np.polyfit(x,R,deg=4)
64         polyGcoeff=np.polyfit(x,G,deg=4)
65         polyBcoeff=np.polyfit(x,B,deg=4)
66     elif color=='grey':
67         R=np.array([0,209,220,230,239,255])/256
68         G=np.array([0,0,89,160,200,255])/256
69         B=np.array([0,154,182,211,229,255])/256
70         x=np.array([0,2.2,2.9,3.7,4.2,5])/5
71         RGB=(R+G+B)/3
72         R,G,B,A=RGB,RGB,RGB,RGB
73         polyRGBcoeff=np.polyfit(x,RGB,deg=4)
74         polyRcoeff=polyRGBcoeff
75         polyGcoeff=polyRGBcoeff
76         polyBcoeff=polyRGBcoeff
77     else:
78         print("Please choose color from: 'seeblau','magenta' or 'grey' ")
79
80     xx=np.linspace(0,1,256)
81     polyRcoeff=np.polyfit(x,R,deg=4)
82     polyGcoeff=np.polyfit(x,G,deg=4)
83     polyBcoeff=np.polyfit(x,B,deg=4)
84     polyR=np.poly1d(polyRcoeff)(xx)
85     polyG=np.poly1d(polyGcoeff)(xx)
86     polyB=np.poly1d(polyBcoeff)(xx)
87     mapped=np.array([polyR.T,polyG.T,
88                      polyB.T,np.ones(256).T]).T
89     mapped[mapped<=0]=0
90     mapped[mapped>=1]=1
91     cpd_img=ListedColormap(mapped)
92     if inverse is not False:
93         cpd_img=ListedColormap(np.flip(mapped, axis=0))
94     return cpd_img

```

List of Figures

1	Scheme of singlet and triplet Cooper pair states	1
2	Schematic of the Polder susceptibility and simulation of the resonance frequency	3
3	Cross-section schematic of a CPW	5
4	Magnetic field distribution of a CPW	6
5	Schematics of the sample designs	9
6	Schematics of the two setups	10
7	Sample holder pictures	11
8	Raw and normalized transmission of sample CPW2	14
9	Normalized transmission and minima of CPW2 and CPW3	15
10	Comparison between different noise reduction methods for transmission data of sample CPW2	17
11	Normalized transmission data in down and up sweep direction	18
12	Normalized transmission of sample CPW1 at the setups HelioxVL and BlueFors	19
13	Normalized transmission of sample CPW2 in frequency and magnetic field sweep method	21
14	Normalized transmission over frequency and as well as temperature over time	22
15	Reflection parameters as a function of resonator length	24
16	Transmission behavior of sample CPW3 over temperature during warm-up	25
17	Typical warm-up curve for the BlueFors setup	26
18	Normalized transmission of samples CPW2 and CPW3	29
19	Fitted transmission minima of samples CPW2 and CPW3	29
20	Averaged transmission of different normalized data of sample CPW2	ii
21	Normalized transmission measured without and with pre-amplifier of sample CPW3	ii

List of Tables

1	Devices used at BlueFors or HelioxVL setup	10
2	Preparation steps of sample CPW2	iii
3	Differences in data acquisition for the samples CPW2 and CPW3	iii

References

- [1] J. Bardeen, L. N. Cooper, and J. R. Schrieffer. "Theory of Superconductivity". In: *Phys. Rev.* 108 (5 Dec. 1957), pp. 1175–1204. DOI: [10.1103/PhysRev.108.1175](https://doi.org/10.1103/PhysRev.108.1175).
- [2] Peter Fulde and Richard A. Ferrell. "Superconductivity in a Strong Spin-Exchange Field". In: *Phys. Rev.* 135 (3A Aug. 1964), A550–A563. DOI: [10.1103/PhysRev.135.A550](https://doi.org/10.1103/PhysRev.135.A550).
- [3] A. I. Larkin and Yu. N. Ovchinnikov. "Quasiclassical Method in the Theory of Superconductivity". In: *Soviet Journal of Experimental and Theoretical Physics* 28 (June 1969), p. 1200.
- [4] R. S. Keizer, S. T. B. Goennenwein, T. M. Klapwijk, G. Miao, G. Xiao, and A. Gupta. "A spin triplet supercurrent through the half-metallic ferromagnet CrO₂". In: *Nature* 439 (2006). DOI: [10.1038/nature04499](https://doi.org/10.1038/nature04499).
- [5] J. W. A. Robinson, J. D. S. Witt, and M. G. Blamire. "Controlled Injection of Spin-Triplet Supercurrents into a Strong Ferromagnet". In: *Science* 329.5987 (2010), pp. 59–61. DOI: [10.1126/science.1189246](https://doi.org/10.1126/science.1189246).
- [6] Yoav Kalcheim, Israel Felner, Oded Millo, Tal Kirzhner, Gad Koren, Angelo Di Bernardo, Mehmet Egilmez, Mark G. Blamire, and J. W. A. Robinson. "Magnetic field dependence of the proximity-induced triplet superconductivity at ferromagnet/superconductor interfaces". In: *Phys. Rev. B* 89 (18 May 2014), p. 180506. DOI: [10.1103/PhysRevB.89.180506](https://doi.org/10.1103/PhysRevB.89.180506).
- [7] Matthias Eschrig. "Spin-polarized supercurrents for spintronics: A review of current progress". In: *Reports on progress in physics. Physical Society (Great Britain)* 78 (Sept. 2015). DOI: [10.1088/0034-4885/78/10/104501](https://doi.org/10.1088/0034-4885/78/10/104501).
- [8] S. Takahashi, S. Hikino, M. Mori, J. Martinek, and S. Maekawa. "Supercurrent Pumping in Josephson Junctions with a Half-Metallic Ferromagnet". In: *Phys. Rev. Lett.* 99 (5 Aug. 2007), p. 057003. DOI: [10.1103/PhysRevLett.99.057003](https://doi.org/10.1103/PhysRevLett.99.057003).
- [9] S Hikino, M Mori, S Takahashi, and S Maekawa. "Microwave-induced supercurrent in a ferromagnetic Josephson junction". In: *Superconductor Science and Technology* 24.2 (Jan. 2011), p. 024008. DOI: [10.1088/0953-2048/24/2/024008](https://doi.org/10.1088/0953-2048/24/2/024008).
- [10] K-R Jeon, C Ciccarelli, AJ Ferguson, H Kurebayashi, L Cohen, X Montiel, M Eschrig, JWA Robinson, and MG Blamire. "Enhanced spin pumping into superconductors provides evidence for superconducting pure spin currents". In: *Nature Materials* 17 (2018), pp. 499–503. DOI: [10.1038/s41563-018-0058-9](https://doi.org/10.1038/s41563-018-0058-9).
- [11] L. Landau and E. Lifshitz. "On the theory of the dispersion of magnetic permeability in ferromagnetic bodies". In: *Perspectives in Theoretical Physics*. Amsterdam: Pergamon, 1992, pp. 51–65. ISBN: 978-0-08-036364-6. DOI: [10.1016/B978-0-08-036364-6.50008-9](https://doi.org/10.1016/B978-0-08-036364-6.50008-9).
- [12] T. L. Gilbert. "A phenomenological theory of damping in ferromagnetic materials". In: *IEEE Transactions on Magnetics* 40.6 (2004), pp. 3443–3449. DOI: [10.1109/TMAG.2004.836740](https://doi.org/10.1109/TMAG.2004.836740).
- [13] J.-M. Beaujour, D. Ravelosona, I. Tudosa, E. E. Fullerton, and A. D. Kent. "Ferromagnetic resonance linewidth in ultrathin films with perpendicular magnetic anisotropy". In: *Physical Review B* 80.18 (Nov. 2009). ISSN: 1550-235X. DOI: [10.1103/physrevb.80.180415](https://doi.org/10.1103/physrevb.80.180415).

- [14] A.G. Gurevich and G.A. Melkov. *Magnetization Oscillations and Waves*. Taylor & Francis, 1996. ISBN: 9780849394607.
- [15] M. L. Schneider, J. M. Shaw, A. B. Kos, Th. Gerrits, T. J. Silva, and R. D. McMichael. "Spin dynamics and damping in nanomagnets measured directly by frequency-resolved magneto-optic Kerr effect". In: *Journal of Applied Physics* 102.10 (2007), p. 103909. DOI: 10.1063/1.2812541. eprint: <https://doi.org/10.1063/1.2812541>.
- [16] Sangita Kalarickal, Pavol Krivosik, Mingzhong Wu, Carl Patton, Michael Schneider, Pavel Kabos, Tom Silva, and J. Nibarger. "Ferromagnetic resonance linewidth in metallic thin films. Comparison of measurement methods". In: *Journal of Applied Physics - J APPL PHYS* 99 (May 2006). DOI: 10.1063/1.2197087.
- [17] Charles Kittel. *Introduction to Solid State Physics*. 7th. John Wiley & Sons, Inc., 1996.
- [18] Chiung-Wu Su, Hong Ho, C. Shern, and R. Chen. "Changes in the Magnetic Anisotropy of Co Thin Films on Pt(111) Capped by Ag Overlayers". In: *Chinese Journal of Physics - CHIN J PHYS* 41 (Oct. 2003).
- [19] N. W. E. McGee, M. T. Johnson, J. J. de Vries, and J. aan de Stegge. "Localized Kerr study of the magnetic properties of an ultrathin epitaxial Co wedge grown on Pt(111)". In: *Journal of Applied Physics* 73.7 (1993), pp. 3418–3425. DOI: 10.1063/1.352943.
- [20] B. Ujfalussy, L. Szunyogh, P. Bruno, and P. Weinberger. "First-Principles Calculation of the Anomalous Perpendicular Anisotropy in a Co Monolayer on Au(111)". In: *Phys. Rev. Lett.* 77 (9 Aug. 1996), pp. 1805–1808. DOI: 10.1103/PhysRevLett.77.1805.
- [21] "Anomalous perpendicular magnetic anisotropy in a Co monolayer on Au(111)". In: *Journal of Magnetism and Magnetic Materials* 165.1 (1997). Symposium E: Magnetic Ultrathin Films, Multilayers and Surfaces, pp. 254–257. ISSN: 0304-8853. DOI: 10.1016/S0304-8853(96)00522-7.
- [22] Sandor Caplan and Gerald Chanin. "Critical-Field Study of Superconducting Aluminum". In: *Phys. Rev.* 138 (5A May 1965), A1428–A1433. DOI: 10.1103/PhysRev.138.A1428.
- [23] P. M. Tedrow and R. Meservey. "Critical magnetic field of very thin superconducting aluminum films". In: *Phys. Rev. B* 25 (1 Jan. 1982), pp. 171–178. DOI: 10.1103/PhysRevB.25.171.
- [24] Olle Karlqvist. "Calculation of the magnetic field in the ferromagnetic layer of a magnetic drum". In: (1954).
- [25] B.C. Wadell. *Transmission Line Design Handbook*. ARTECH HOUSE ANTENNAS AND PROPAGATION LIBRARY. Artech House, 1991. ISBN: 9780890064368.
- [26] "Conventional Coplanar Waveguide". In: *Coplanar Waveguide Circuits, Components, and Systems*. John Wiley & Sons, Ltd, 2001. Chap. 2, pp. 11–86. ISBN: 9780471224754. DOI: 10.1002/0471224758.ch2.
- [27] A. Buzdin and Valeriy Ryazanov. "Proximity effect in superconductorferromagnet heterostructures". In: *Comptes Rendus Physique* 7 (Jan. 2006), pp. 107–115. DOI: 10.1016/j.crhy.2005.12.006.
- [28] Daniel Gall. "Electron mean free path in elemental metals". In: *Journal of Applied Physics* 119 (Feb. 2016), p. 085101. DOI: 10.1063/1.4942216.
- [29] A. Aharoni and R.K.P.T.M.A. Aharoni. *Introduction to the Theory of Ferromagnetism*. International series of monographs on physics. Oxford University Press, 2000. ISBN: 9780198508083.
- [30] F Bergeret, A. Volkov, and Konstantin Efetov. "Long-Range Proximity Effects in Super Conductor-Ferromagnet Structures". In: *Physical review letters* 86 (May 2001), pp. 4096–9. DOI: 10.1103/PhysRevLett.86.4096.

- [31] R Kleiner W. Buckel. *Josephsonkontakte und ihre Eigenschaften*. John Wiley & Sons, Ltd, 2013. Chap. 6, pp. 327–379. ISBN: 9783527668670. DOI: 10.1002/9783527668670.ch6.
- [32] Hannes Maier-Flaig, Sebastian T. B. Goennenwein, Ryo Ohshima, Masashi Shiraishi, Rudolf Gross, Hans Huebl, and Mathias Weiler. “Note: Derivative divide, a method for the analysis of broadband ferromagnetic resonance in the frequency domain”. In: *Review of Scientific Instruments* 89.7 (2018), p. 076101. DOI: 10.1063/1.5045135.
- [33] Hannes Benjamin Maier-Flaig. *Magnetic resonance of ferrimagnetic insulators*. Technische Universität München, 2017.
- [34] S. Tamaru, S. Tsunegi, H. Kubota, and S. Yuasa. “Vector network analyzer ferromagnetic resonance spectrometer with field differential detection”. In: *Review of Scientific Instruments* 89.5 (2018), p. 053901. DOI: 10.1063/1.5022762.
- [35] I. Harward, T. O’Keevan, A. Hutchison, V. Zagorodnii, and Z. Celinski. “A broadband ferromagnetic resonance spectrometer to measure thin films up to 70 GHz”. In: *Review of Scientific Instruments* 82.9 (2011), p. 095115. DOI: 10.1063/1.3641319.
- [36] V. P. Denysenkov and A. M. Grishin. “Broadband ferromagnetic resonance spectrometer”. In: *Review of Scientific Instruments* 74.7 (2003), pp. 3400–3405. DOI: 10.1063/1.1581395.
- [37] C. Bilzer, T. Devolder, P. Crozat, C. Chappert, S. Cardoso, and P. P. Freitas. “Vector network analyzer ferromagnetic resonance of thin films on co-planar waveguides: Comparison of different evaluation methods”. In: *Journal of Applied Physics* 101.7 (2007), p. 074505. DOI: 10.1063/1.2716995.
- [38] BlueFors Cryogenics. *BF-LD400 Cryogen-free Dilution Refrigerator System*. Version 1.4.0. 2013.
- [39] Inc. American Magnetics. *Model 430 Power Supply Programmer*. 2017.
- [40] Inc. Lake Shore Cryotronics. *Model 370 AC Resistance Bridge*. 2009.
- [41] Inc. Lake Shore Cryotronics. *Ruthenium Oxide (RoxTM) RTDs*.
- [42] Oxford Instruments. *Heliox Sorption Pumped He-3 Refrigerator Systems*. 2013.
- [43] Oxford Instruments. *IPS120-10 Superconducting Magnet Power Supplies*. 2000.
- [44] Inc. Lake Shore Cryotronics. *Cernox RTDs*.
- [45] Rohde&Schwarz. *R&S ZNB/ZNBT Vector Network Analyzers, User Manual*. Version 52. 2020.
- [46] Rohde&Schwarz. *R&S ZNB/ZNBT Vector Network Analyzers, Specifications*. Version 13. 2021.
- [47] Rohde&Schwarz. *R&S ZNB/ZNBT Vector Network Analyzers, Product Brochure*. Version 9. 2020.
- [48] Keysight Technologies. *Keysight U7227A/C/F USB Pre-Amplifier*. 5th ed. 2019.
- [49] Greisinger electronic GmbH. *GIA 2000 / GIR 2002*. Version 2.8.
- [50] Greisinger electronic GmbH. *GMH3xxx - Serial Interface*. 2004.
- [51] Philip Dominic Louis. *Broadband-Spectroscopy of Magnetic Materials at Low Temperatures*. Technische Universität München, 2016.
- [52] Luise Siegl. *Spin Dynamics in Magnetic Garnets by Broadband Ferromagnetic Resonance Measurements*. Technische Universität Dresden, 2020.
- [53] W. Barry. “A Broad-Band, Automated, Stripline Technique for the Simultaneous Measurement of Complex Permittivity and Permeability”. In: *IEEE Transactions on Microwave Theory and Techniques* 34.1 (1986), pp. 80–84. DOI: 10.1109/TMTT.1986.1133283.

- [54] Rafael C. Gonzalez and Richard E. Woods. *Digital image processing*. Prentice Hall, 2008.
- [55] R. L. Smith-Rose. "The Electrical Properties of Soil for Alternating Currents at Radio Frequencies". In: *Proceedings of the Royal Society of London. Series A, Containing Papers of a Mathematical and Physical Character* 140.841 (1933), pp. 359–377. ISSN: 09501207.
- [56] H. Vanhamme. "High resolution frequency-domain reflectometry". In: *IEEE Transactions on Instrumentation and Measurement* 39.2 (1990), pp. 369–375. DOI: 10.1109/19.52517.
- [57] Y. -. Shin, E. J. Powers, T. -. Choe, Chan-Young Hong, Eun-Seok Song, Jong-Gwan Yook, and Jin Bae Park. "Application of time-frequency domain reflectometry for detection and localization of a fault on a coaxial cable". In: *IEEE Transactions on Instrumentation and Measurement* 54.6 (2005), pp. 2493–2500. DOI: 10.1109/TIM.2005.858115.
- [58] Keysight Technologies. *Time Domain Analysis Using a Network Analyzer*. 2020.
- [59] HUBER+SUHNER. *Data Sheet SF102*. Aug. 2020.
- [60] elspec GmbH. *Übersicht Semi-Rigid Kabel*. German.
- [61] Tinouche, Kharmouche, Aktas, Yildiz, and Kocabay. "Magnetic and Structural Properties of Co Thin Films Evaporated on GaAs Substrate". In: *Journal of Superconductivity and Novel Magnetism* 28 (Mar. 2015), pp. 921–5. DOI: 10.1007/s10948-014-2863-y.
- [62] Mahdi Jamali, Yang Lv, Zhengyang Zhao, and Jian-Ping Wang. "Sputtering of cobalt film with perpendicular magnetic anisotropy on disorder-free graphene". In: *AIP Advances* 4.10 (2014), p. 107102. DOI: 10.1063/1.4897333.
- [63] M. Aus, C. Cheung, Barbara Szpunar, U. Erb, and Jerzy Szpunar. "Saturation Magnetization of Porosity-free Nanocrystalline Cobalt". In: *Journal of Materials Science Letters* 17 (Jan. 1998), pp. 1949–1952. DOI: 10.1023/A:1006620812602.
- [64] J.M. Alameda, F. Carmona, F.H. Salas, L.M. Alvarez-Prado, R. Morales, and G.T. Pérez. "Effects of the initial stages of film growth on the magnetic anisotropy of obliquely-deposited cobalt thin films". In: *Journal of Magnetism and Magnetic Materials* 154.2 (1996), pp. 249–253. ISSN: 0304-8853. DOI: 10.1016/0304-8853(95)00577-3.
- [65] Allresist GmbH. *Positiv-Photoresists für Lift-off AR-P 5300*. German. 2015.
- [66] Inkscape Documentation Authors. *Inkscape Beginners Guide*. Version 1.0.2. 2020.
- [67] Smart Force Technologies SAS. *BF-LD400 Cryogen-free Dilution Refrigerator System*. Version 1.5. 2018.
- [68] Allresist GmbH. *Entwickler für AR-Resists*. German. 2018.
- [69] Christian Schrim. *Leitwertfluktuationen von Ein-Atom-Kontakten*. German. Universität Konstanz, 2002.

Acknowledgments

First and foremost, I would like to thank Prof. Dr. Elke Scheer for making it possible for me to work on this project. I thank her for her trust and the freedom to work with the setups and equipment. Further I thank for the constructive discussions and helpful suggestions.

I thank Prof. Dr Angelo Di Bernardo for his support as my second reviewer, his fruitful suggestions, and his incredible expertise.

I would like to thank Andreas Bloch for his calm, uncomplicated and reflective way of patiently supervising my work. I would also like to thank him for teaching me about sample preparation, the technique for transport measurements and the operation of the HelioxVL setup.

Furthermore, I would like to thank Sergej Andreev, who introduced me to FMR technique at low temperatures. Likewise for the introduction to the measurement wiring, control and repair of the BlueFors setup.

At this point I would also like to thank Martin Prestel for the introduction for cooling down the BlueFors to base temperature. My thanks also go to Lukas Kammermeier and Roman Hartmann for their help with programming and sample preparation.

I would also like to thank the whole working group for the most inspiring working atmosphere and the great hours spent together at lunch and coffee break. Thank you Guyse!

Ich möchte mich bei meinen Kommilitonen und Freunden Jacob, Daniel und Michael, für den Beistand und die vielen gemeinsamen nerdigen Stunden in den letzten Jahren bedanken.

Danki Anki, für deine Hilfe und Unterstützung, auch Abseits dieser Arbeit.

Danke an meine Familie, für diese unglaubliche Chance, die endlose Unterstützung und das tiefe Vertrauen, dass mein Weg der Richtige sein wird. Danke euch Dreien!

Danke an alle, die mir eine Fortsetzung meines Weges ermöglichen!

The Road not Taken¹

...

Two roads diverged in a wood, and I—
I took the one less traveled by,
And that has made all the difference.

¹Robert Frost (*1874, †1963)